Comput. Methods Appl. Mech. Engrg. 198 (2009) 3130–3150

Contents lists available at ScienceDirect

Comput. Methods Appl. Mech. Engrg.

journal homepage: www.elsevier.com/locate/cma

A discontinuous Galerkin solver for Boltzmann–Poisson systems in nano devices ☆

Yingda Cheng [a], Irene M. Gamba [a,*,1], Armando Majorana [b,2], Chi-Wang Shu [c,3]

[a] Department of Mathematics and ICES, University of Texas, Austin, TX 78712, United States
[b] Dipartimento di Matematica e Informatica, Università di Catania, Catania, Italy
[c] Division of Applied Mathematics, Brown University, Providence, RI 02912, United States

ARTICLE INFO

Article history:
Received 9 February 2009
Received in revised form 18 May 2009
Accepted 21 May 2009
Available online 3 June 2009

Keywords:
Deterministic numerical methods
Discontinuous Galerkin schemes
Boltzmann–Poisson systems
Statistical hot electron transport
Semiconductor nano-scale devices

ABSTRACT

In this paper, we present results of a discontinuous Galerkin (DG) scheme applied to deterministic computations of the transients for the Boltzmann–Poisson system describing electron transport in semiconductor devices. The collisional term models optical-phonon interactions which become dominant under strong energetic conditions corresponding to nano-scale active regions under applied bias. The proposed numerical technique is a finite element method using discontinuous piecewise polynomials as basis functions on unstructured meshes. It is applied to simulate hot electron transport in bulk silicon, in a silicon n^+—n—n^+ diode and in a double gated 12 nm MOSFET. Additionally, the obtained results are compared to those of a high order WENO scheme simulation and DSMC (Discrete Simulation Monte Carlo) solvers.

1. Introduction

The evolution of the electron distribution function $f(t,\mathbf{x},\mathbf{k})$ in semiconductors in dependence of time t, position $\mathbf{x}$ and electron wave vector $\mathbf{k}$ is governed by the Boltzmann transport equation (BTE) [24,28,21]

$$\frac{\partial f}{\partial t}+\frac{1}{\hbar}\nabla_{\mathbf{k}}\varepsilon\cdot\nabla_{\mathbf{x}}f-\frac{q}{\hbar}\mathbf{E}\cdot\nabla_{\mathbf{k}}f=Q(f), \tag{1.1}$$

where $\hbar$ is the reduced Planck constant, and q denotes the positive elementary charge. The function $\varepsilon(\mathbf{k})$ is the energy of the considered crystal conduction band measured from the band minimum; according to the Kane dispersion relation, ε is the positive root of

$$\varepsilon(1+\alpha\varepsilon)=\frac{\hbar^2k^2}{2m^*}, \tag{1.2}$$

where α is the non-parabolicity factor and m^* the effective electron mass. The electric field $\mathbf{E}$ is related to the doping density N_D and the electron density n, which equals the zero-order moment of the electron distribution function f, by the Poisson equation

$$\nabla_{\mathbf{x}}[\epsilon_r(\mathbf{x})\nabla_{\mathbf{x}}V]=\frac{q}{\epsilon_0}[n(t,\mathbf{x})-N_D(\mathbf{x})],\quad \mathbf{E}=-\nabla_{\mathbf{x}}V, \tag{1.3}$$

where ϵ_0 is the dielectric constant of the vacuum, $\epsilon_r(\mathbf{x})$ labels the relative dielectric function depending on the material and V the electrostatic potential. The collision operator $Q(f)$ takes into account acoustic deformation potential and optical intervalley scattering [31,29]. For low electron densities, it reads

$$Q(f)(t,\mathbf{x},\mathbf{k})=\int_{\mathbb{R}^3}[S(\mathbf{k}',\mathbf{k})f(t,\mathbf{x},\mathbf{k}')-S(\mathbf{k},\mathbf{k}')f(t,\mathbf{x},\mathbf{k})]d\mathbf{k}' \tag{1.4}$$

with the scattering kernel

$$\begin{aligned}S(\mathbf{k},\mathbf{k}')=&(n_q+1)K\delta(\varepsilon(\mathbf{k}')-\varepsilon(\mathbf{k})+\hbar\omega_p)+n_qK\delta(\varepsilon(\mathbf{k}')-\varepsilon(\mathbf{k})-\hbar\omega_p)\\&+K_0\delta(\varepsilon(\mathbf{k}')-\varepsilon(\mathbf{k}))\end{aligned} \tag{1.5}$$

and K and K_0 being constant for silicon. The symbol δ indicates the usual Dirac distribution and ω_p is the constant phonon frequency. Moreover,

$$n_q=\left[\exp\left(\frac{\hbar\omega_p}{k_BT_L}\right)-1\right]^{-1}$$

is the occupation number of phonons, k_B is the Boltzmann constant and T_L is the constant lattice temperature.

Semiclassical description of electron flow in semiconductors is an equation in six dimensions (plus time if the device is not in steady state) for a truly 3-D device, and four dimensions for a

☆ Support from the Institute of Computational Engineering and Sciences and the University of Texas Austin is gratefully acknowledged.

* Corresponding author.
E-mail addresses: ycheng@math.utexas.edu (Y. Cheng), gamba@math.utexas.edu (I.M. Gamba), majorana@dmi.unict.it (A. Majorana), shu@dam.brown.edu (C.-W. Shu).

[1] Research supported by NSF-0807712 and NSF-FRG-0757450.
[2] Research supported by Italian PRIN 2006: Kinetic and continuum models for particle transport in gases and semiconductors: analytical and computational aspects.
[3] Research supported by NSF Grant DMS-0809086 and DOE Grant DE-FG02-08ER25863.

0045-7825/$ - see front matter © 2009 Elsevier B.V. All rights reserved.
doi:10.1016/j.cma.2009.05.015

1-D device. This heavy computational cost explains why the BP system is traditionally simulated by the Direct Simulation Monte Carlo (DSMC) methods [23]. In recent years, deterministic solvers to the BP system were proposed [20,27,3,2,4–6,22]. These methods provide accurate results which, in general, agree well with those obtained from Monte Carlo (DSMC) simulations, often at a fractional computational time. Moreover, they can resolve transient details for the *pdf*, which are difficult to compute with DSMC simulators. The methods proposed in [4,6] used weighted essentially non-oscillatory (WENO) finite difference schemes to solve the Boltzmann–Poisson system. The advantage of the WENO scheme is that it is relatively simple to code and very stable even on coarse meshes for solutions containing sharp gradient regions. A disadvantage of the WENO finite difference method is that it requires smooth meshes to achieve high order accuracy, hence it is not very flexible for adaptive meshes.

On the other hand, motivated by the easy *hp*-adaptivity and simple communication pattern of the discontinuous Galerkin (DG) methods for macroscopic (fluid level) models [7,8,25,26], we proposed in [11,10] to implement a DG solver to the full Boltzmann equation, that is capable of capturing transients of the probability density function (*pdf*).

The type of DG method that we will discuss here is a class of finite element methods originally devised to solve hyperbolic conservation laws containing only first order spatial derivatives, e.g. [16,15,14,13,17]. Using completely discontinuous polynomial space for both the test and trial functions in the spatial variables and coupled with explicit and nonlinearly stable high order Runge–Kutta time discretization, the method has the advantage of flexibility for arbitrarily unstructured meshes, with a compact stencil, and with the ability to easily accommodate arbitrary *hp*-adaptivity. For more details about DG scheme for convection dominated problems, we refer to the review paper [19]. The DG method was later generalized to the local DG (LDG) method to solve the convection diffusion equation [18] and elliptic equations [1]. It is L^2 stable and locally conservative, which makes it particularly suitable to treat the Poisson equation.

In our previous preliminary work [11,10], we proposed the first DG solver for (1.1) and showed some numerical calculations for one- and two-dimensional devices. In this paper, we will carefully formulate the DG-LDG scheme for the Boltzmann–Poisson system and perform extensive numerical studies to validate our calculation. In addition, using this new scheme, we are able to implement a solver to full energy bands [9] that no other deterministic solver has been able to implement so far. It would be more difficult or even unpractical to produce the full band computation with other transport scheme.

This paper is organized as follows: in Section 2, we review the change of variables in [27,5]. In Section 3, we study the DG-BTE solver for 1D diodes. Section 4 is devoted to the discussion of the 2D double gate MOSFET DG solver. Conclusions and final remarks are presented in Section 5. Some technical implementations of the DG solver are collected in Appendix A.

2. Change of variables

In this section, we review the change of variables proposed in [27,4].

For the numerical treatment of the system (1.1) and (1.3), it is convenient to introduce suitable dimensionless quantities and variables. We assume $T_L = 300$ K. Typical values for length, time and voltage are $\ell_* = 10^{-6}$ m, $t_* = 10^{-12}$ s and $V_* = 1$ V, respectively. Thus, we define the dimensionless variables

$$(x,y) = \frac{\mathbf{x}}{\ell_*}, \quad t = \frac{t}{t_*}, \quad \Psi = \frac{V}{V_*}, \quad (E_x, E_y, 0) = \frac{\mathbf{E}}{E_*}$$

with $E_* = 0.1 V_* \ell_*^{-1}$ and

$$E_x = -c_v \frac{\partial \Psi}{\partial x}, \quad E_y = -c_v \frac{\partial \Psi}{\partial y}, \quad c_v = \frac{V_*}{\ell_* E_*}.$$

In correspondence to [27,5], we perform a coordinate transformation for $\mathbf{k}$ according to

$$\mathbf{k} = \frac{\sqrt{2m^* k_B T_L}}{\hbar} \sqrt{w(1+\alpha_K w)} \left(\mu, \sqrt{1-\mu^2}\cos\varphi, \sqrt{1-\mu^2}\sin\varphi \right), \tag{2.6}$$

where the new independent variables are the dimensionless energy $w = \frac{\varepsilon}{k_B T_L}$, the cosine of the polar angle μ and the azimuth angle φ with $\alpha_K = k_B T_L \alpha$. The main advantage of the generalized spherical coordinates (2.6) is the easy treatment of the Dirac distribution in the kernel (1.5) of the collision term. In fact, this procedure enables us to transform the integral operator (1.4) with the nonregular kernel S into an integral-difference operator, as shown in the following.

We are interested in studying problems that are two-dimensional in real space and three-dimensional in $\mathbf{k}$-space. It would be useful to consider the new unknown function Φ related to the electron distribution function via

$$\Phi(t,x,y,w,\mu,\varphi) = s(w) f(t,\mathbf{x},\mathbf{k}),$$

where

$$s(w) = \sqrt{w(1+\alpha_K w)}(1+2\alpha_K w) \tag{2.7}$$

is proportional to the Jacobian of the change of variables (2.6) and, apart from a dimensional constant factor, to the density of states. This allows us to write the free streaming operator of the dimensionless Boltzmann equation in a conservative form, which is appropriate for applying standard numerical schemes used for hyperbolic partial differential equations. Due to the symmetry of the problem and of the collision operator, we have

$$\Phi(t,x,y,w,\mu,2\pi-\varphi) = \Phi(t,x,y,w,\mu,\varphi). \tag{2.8}$$

Straightforward but cumbersome calculations end in the following transport equation for Φ:

$$\frac{\partial \Phi}{\partial t} + \frac{\partial}{\partial x}(g_1 \Phi) + \frac{\partial}{\partial y}(g_2 \Phi) + \frac{\partial}{\partial w}(g_3 \Phi) + \frac{\partial}{\partial \mu}(g_4 \Phi) + \frac{\partial}{\partial \varphi}(g_5 \Phi) = C(\Phi). \tag{2.9}$$

The functions g_i $(i = 1,2,\ldots,5)$ in the advection terms depend on the independent variables w, μ, φ as well as on time and position via the electric field. They are given by

$$g_1(\cdot) = c_x \frac{\mu\sqrt{w(1+\alpha_K w)}}{1+2\alpha_K w},$$

$$g_2(\cdot) = c_x \frac{\sqrt{1-\mu^2}\sqrt{w(1+\alpha_K w)}\cos\varphi}{1+2\alpha_K w},$$

$$g_3(\cdot) = -2c_k \frac{\sqrt{w(1+\alpha_K w)}}{1+2\alpha_K w}\left[\mu E_x(t,x,y) + \sqrt{1-\mu^2}\cos\varphi E_y(t,x,y)\right],$$

$$g_4(\cdot) = -c_k \frac{\sqrt{1-\mu^2}}{\sqrt{w(1+\alpha_K w)}}\left[\sqrt{1-\mu^2}E_x(t,x,y) - \mu\cos\varphi E_y(t,x,y)\right],$$

$$g_5(\cdot) = c_k \frac{\sin\varphi}{\sqrt{w(1+\alpha_K w)}\sqrt{1-\mu^2}} E_y(t,x,y)$$

with

$$c_x = \frac{t_*}{\ell_*}\sqrt{\frac{2k_B T_L}{m^*}} \quad \text{and} \quad c_k = \frac{t_* q E_*}{\sqrt{2m^* k_B T_L}}.$$

The right hand side of (2.9) is the integral-difference operator

$$C(\Phi)(t,x,y,w,\mu,\varphi) = s(w)\Big\{c_0\int_0^{\pi}d\varphi'\int_{-1}^{1}d\mu'\Phi(t,x,y,w,\mu',\varphi') + \int_0^{\pi}d\varphi'\int_{-1}^{1}d\mu'[c_+\Phi(t,x,y,w+\gamma,\mu',\varphi') + c_-\Phi(t,x,y,w-\gamma,\mu',\varphi')]\Big\} - 2\pi[c_0 s(w) + c_+ s(w-\gamma) + c_- s(w+\gamma)]\Phi(t,x,y,w,\mu,\varphi),$$

where

$$(c_0,c_+,c_-) = \frac{2m^* t_*}{\hbar^3}\sqrt{2m^* k_B T_L}(K_0,(n_q+1)K,n_q K), \quad \gamma = \frac{\hbar\omega_p}{k_B T_L}$$

are dimensionless parameters. We remark that the δ distributions in the kernel S have been eliminated which leads to the shifted arguments of Φ. The parameter γ represents the jump constant corresponding to the quantum of energy $\hbar\omega_p$. We have also taken into account (2.8) in the integration with respect to φ'. Since the energy variable ω is not negative, we must consider null Φ and the function s, if the argument $\omega-\gamma$ is negative.

In terms of the new variables the electron density becomes

$$n(t_* t,\ell_* x,\ell_* y) = \int_{\mathbb{R}^3} f(t_* t,\ell_* x,\ell_* y,\mathbf{k})d\mathbf{k} = \left(\frac{\sqrt{2m^* k_B T_L}}{\hbar}\right)^3 \rho(t,x,y),$$

where

$$\rho(t,x,y) = \int_0^{+\infty} dw\int_{-1}^{1}d\mu\int_0^{\pi}d\varphi\Phi(t,x,y,w,\mu,\varphi). \tag{2.10}$$

Hence, the dimensionless Poisson equation is

$$\frac{\partial}{\partial x}\left(\epsilon_r\frac{\partial\Psi}{\partial x}\right) + \frac{\partial}{\partial y}\left(\epsilon_r\frac{\partial\Psi}{\partial y}\right) = c_p[\rho(t,x,y) - \mathcal{N}_D(x,y)] \tag{2.11}$$

with

$$\mathcal{N}_D(x,y) = \left(\frac{\sqrt{2m^* k_B T_L}}{\hbar}\right)^{-3} N_D(\ell_* x,\ell_* y) \quad \text{and}$$

$$c_p = \left(\frac{\sqrt{2m^* k_B T_L}}{\hbar}\right)^3 \frac{\ell_*^2 q}{\epsilon_0}.$$

Choosing the same values of the physical parameters as in [27], we obtain

$c_0 \approx 0.26531$	$c_x \approx 0.16857$	$c_p \approx 1830349$
$c_+ \approx 0.50705$	$c_k \approx 0.32606$	$c_v = 10$
$c_- \approx 0.04432$	$\gamma \approx 2.43723$	$\alpha_K \approx 0.01292$
$\epsilon_r = 11.7$		

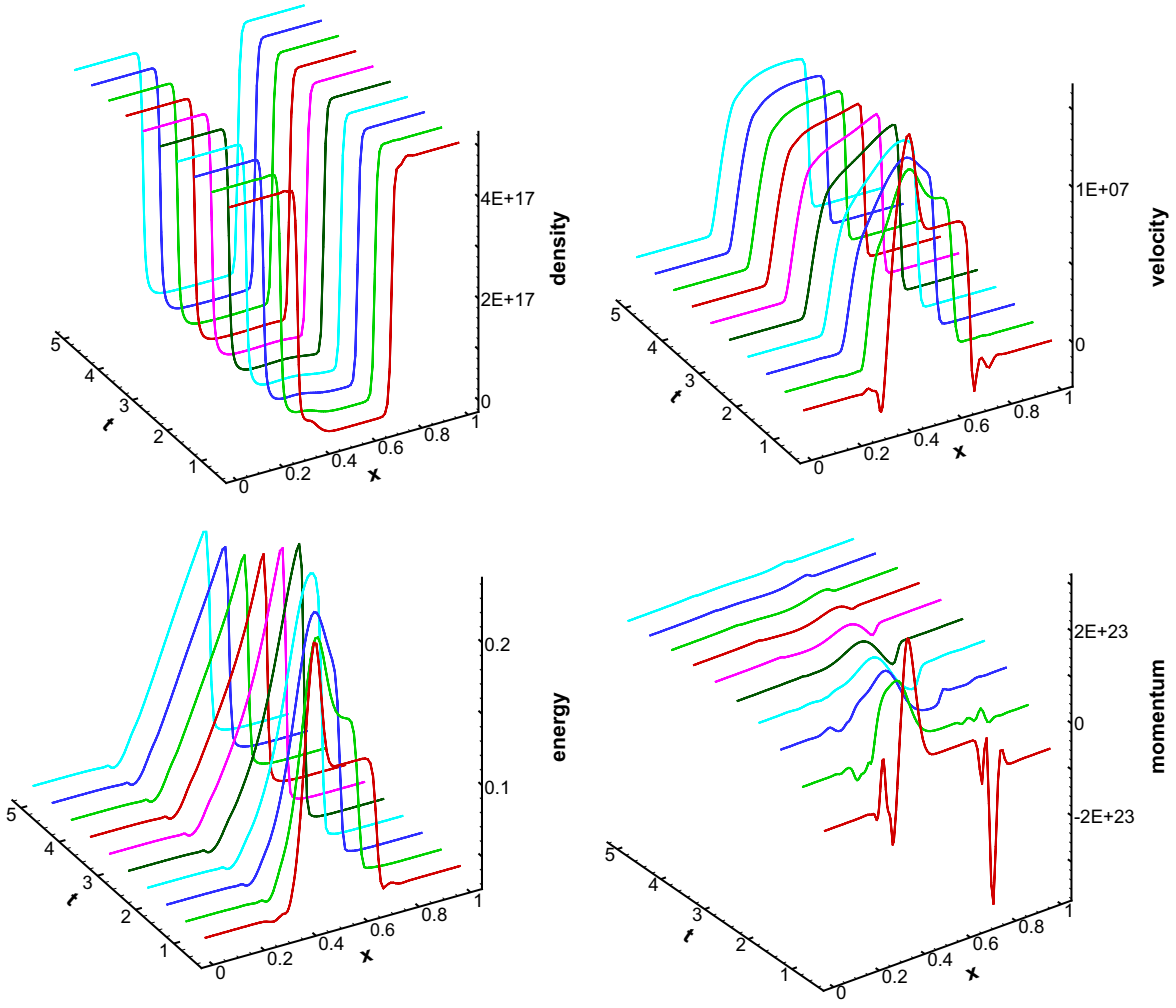

Fig. 3.1. Time evolution of macroscopic quantities using DG method for 400 nm channel at $V_{\text{bias}} = 1.0$ V. Top left: density in cm^{-3}; top right: mean velocity in cm/s; bottom left: energy in eV; bottom right: momentum in cm^{-2} s^{-1}.

Moreover, the dimensional x-component of the velocity is given by

$$\frac{\int_0^{+\infty} dw \int_{-1}^{1} d\mu \int_0^{\pi} d\varphi g_1(w,\mu)\Phi(t,x,y,w,\mu,\varphi)}{\rho(t,x,y)},$$

the dimensional density by

$$1.0115 \times 10^{26} \times \rho(t,x,y),$$

and the energy by

$$0.025849 \times \frac{\int_0^{+\infty} dw \int_{-1}^{1} d\mu \int_0^{\pi} d\varphi w\Phi(t,x,y,w,\mu,\varphi)}{\rho(t,x,y)}.$$

In a simplified model, we consider our device in the $x-$direction by assuming that the doping profile, the potential and thus the force field are only x-dependent. By cylindrical symmetry, the resulting distribution function does not depend on φ. In this case, the Boltzmann transport equation is reduced to

$$\frac{\partial \Phi}{\partial t} + \frac{\partial}{\partial x}(g_1\Phi) + \frac{\partial}{\partial w}(g_3\Phi) + \frac{\partial}{\partial \mu}(g_4\Phi) = C(\Phi). \tag{2.12}$$

with

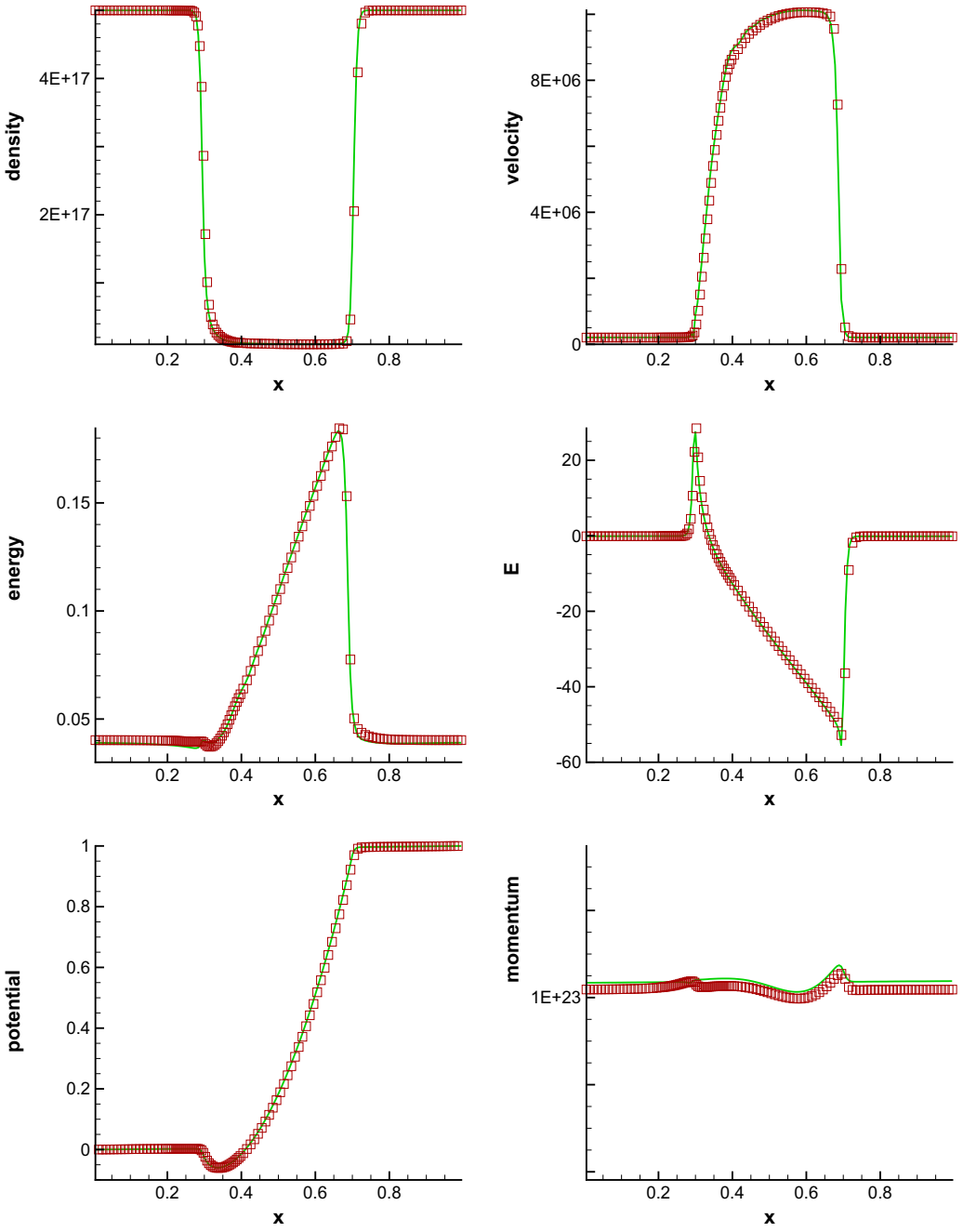

Fig. 3.2. Comparison of macroscopic quantities using DG (symbols) and WENO (solid line) for 400 nm channel at $t = 5.0$ ps, $V_{bias} = 1.0$ V. Top left: density in cm^{-3}; top right: mean velocity in cm/s; middle left: energy in eV; middle right: electric field in kV/cm; bottom left: potential in V; bottom right: momentum in cm^{-2} s^{-1}. Solution has reached steady state.

$$g_1(\cdot) = c_x \frac{\mu\sqrt{w(1+\alpha_K w)}}{1+2\alpha_K w},$$
$$g_3(\cdot) = -2c_k \frac{\sqrt{w(1+\alpha_K w)}}{1+2\alpha_K w}\mu E(t,x),$$
$$g_4(\cdot) = -c_k \frac{1-\mu^2}{\sqrt{w(1+\alpha_K w)}} E(t,x)$$

and

$$C(\Phi)(t,x,w,\mu) = s(w)\Big\{c_0\pi\int_{-1}^{1} d\mu'\Phi(t,x,w,\mu') + \pi\int_{-1}^{1} d\mu'[c_+\Phi(t,x,w+\gamma,\mu') + c_-\Phi(t,x,w-\gamma,\mu')]\Big\} - 2\pi[c_0 s(w) + c_+ s(w-\gamma) + c_- s(w+\gamma)]\Phi(t,x,w,\mu),$$

In terms of the new variables the electron density becomes

$$n(t_*t, \ell_* x) = \int_{\mathbb{R}^3} f(t_*t, \ell_* x, \mathbf{k}) d\mathbf{k} = \left(\frac{\sqrt{2m^* k_B T_L}}{\hbar}\right)^3 \rho(t,x),$$

where

$$\rho(t,x) = \pi\int_0^{+\infty} dw \int_{-1}^{1} d\mu\Phi(t,x,w,\mu). \tag{2.13}$$

Hence, the dimensionless Poisson equation writes

$$\frac{\partial}{\partial x}\left(\epsilon_r \frac{\partial \Psi}{\partial x}\right) = c_p[\rho(t,x) - \mathscr{N}_D(x)] \tag{2.14}$$

and

$$E = -c_v \frac{\partial \Psi}{\partial x}.$$

3. DG-BTE solver for 1D diodes simulation

3.1. Algorithm description

We begin with formulating the DG-BTE solver for 1D diodes. These examples have been thoroughly studied and tested by WENO in [4].

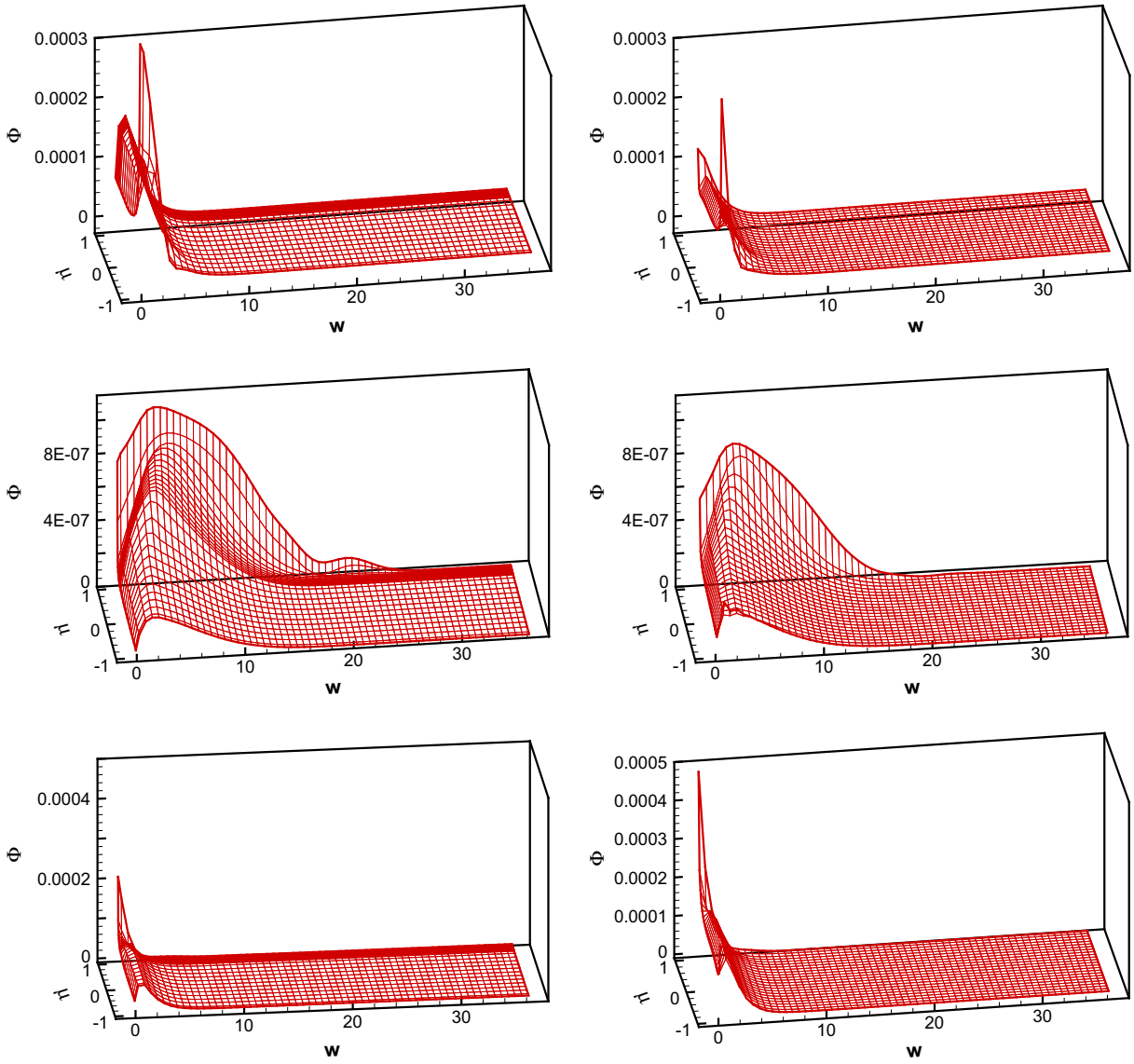

Fig. 3.3. Comparison of the snapshot for $\Phi(x_0, w, \mu)$ using DG (left) and WENO (right) for 400 nm channel at $t = 0.5$ ps, $V_{\text{bias}} = 1.0$ V. Top: $x_0 = 0.3$ μm; middle: $x_0 = 0.5$ μm; bottom: $x_0 = 0.7$ μm. Solution has not yet reached steady state.

The Boltzmann–Poisson system (2.12) and (2.14) will be solved on the domain

$$x \in [0, L], \quad w \in [0, w_{\max}], \quad \mu \in [-1, 1],$$

where L is the dimensionless length of the device and $w_{\max}$ is the maximum value of the energy, which is adjusted in the numerical experiments such that

$$\Phi(t, x, w, \mu) \approx 0 \quad \text{for } w \geqslant w_{\max} \text{ and every } t, x, \mu.$$

In (2.12), g_1 and g_3 are completely smooth in the variable w and μ, assuming E is given and smooth. However, g_4 is singular for the energy $w = 0$, although it is compensated by the $s(w)$ factor in the definition of Φ.

The initial value of f is a locally Maxwellian distribution at the temperature T_L,

$$\Phi(0, x, w, \mu) = s(w) N_D(x) e^{-w} \mathscr{M}$$

with the numerical parameter $\mathscr{M}$ chosen so that the initial value for the density is equal to the doping $N_D(x)$.

We choose to perform our calculations on the following rectangular grid:

$$\Omega_{ikm} = \left[x_{i-\frac{1}{2}}, x_{i+\frac{1}{2}}\right] \times \left[w_{k-\frac{1}{2}}, w_{k+\frac{1}{2}}\right] \times \left[\mu_{m-\frac{1}{2}}, \mu_{m+\frac{1}{2}}\right], \tag{3.15}$$

where $i = 1, \ldots N_x, k = 1, \ldots N_w, m = 1, \ldots N_\mu$, and

$$x_{i\pm\frac{1}{2}} = x_i \pm \frac{\Delta x_i}{2}, \quad w_{k\pm\frac{1}{2}} = w_k \pm \frac{\Delta w_k}{2}, \quad \mu_{m\pm\frac{1}{2}} = \mu_m \pm \frac{\Delta \mu_m}{2}.$$

It is useful that we pick N_μ to be even, so the function g_1 will assume a constant sign in each cell Ω_{ikm}.

The approximation space is thus defined as

$$V_h^\ell = \{v : v|_{\Omega_{ikm}} \in P^\ell(\Omega_{ikm})\}, \tag{3.16}$$

where $P^\ell(\Omega_{ikm})$ is the set of all polynomials of degree at most ℓ on Ω_{ikm}. The DG formulation for the Boltzmann equation (2.12) would be: to find $\Phi_h \in V_h^\ell$, such that

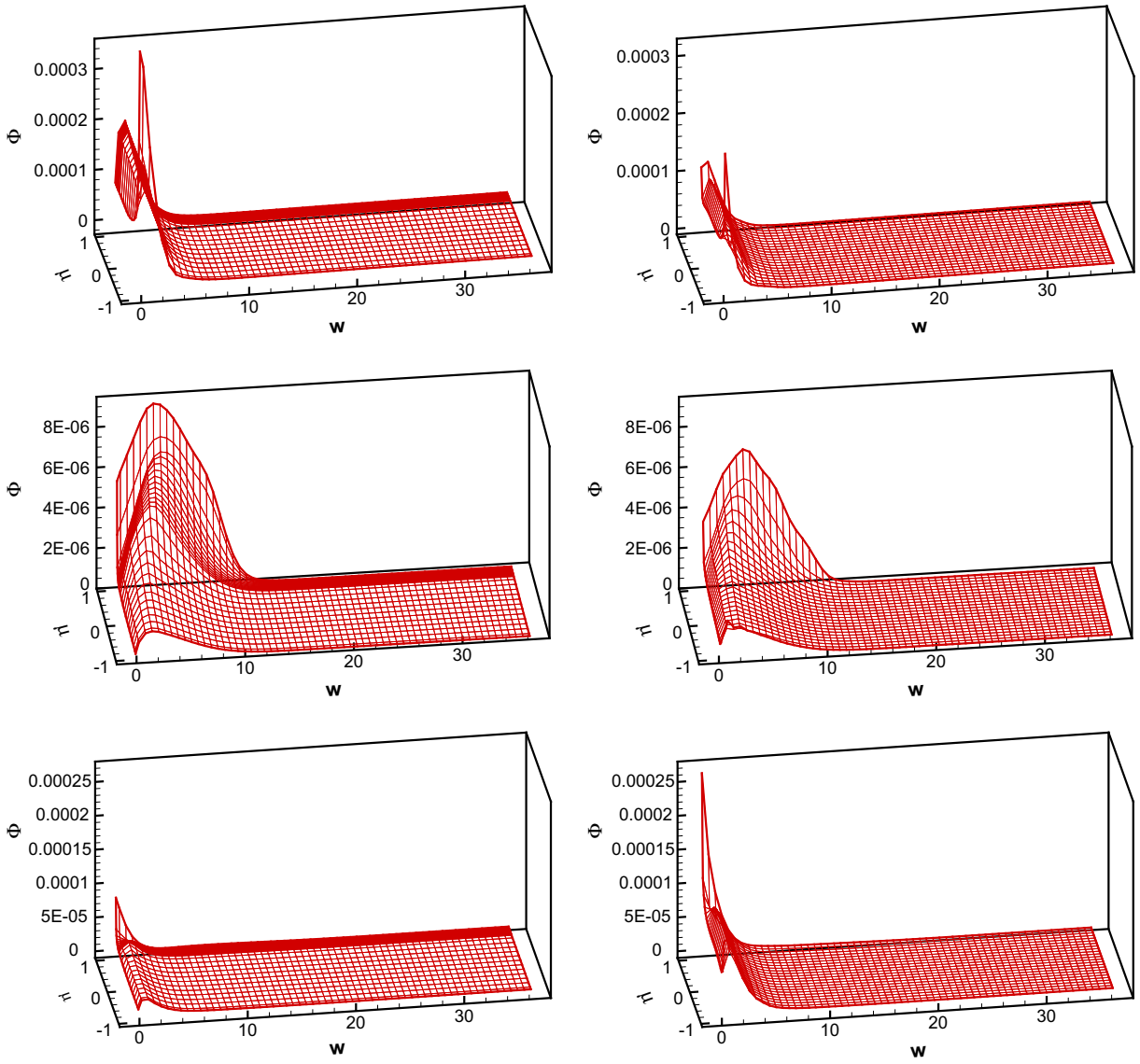

Fig. 3.4. Comparison of the snapshot for $\Phi(x_0, w, \mu)$ using DG (left) and WENO (right) for 400 nm channel at $t = 5.0$ ps, $V_{\text{bias}} = 1.0$ V. Top: $x_0 = 0.3$ μm; middle: $x_0 = 0.5$ μm; bottom: $x_0 = 0.7$ μm. Solution has reached steady state.

$$\int_{\Omega_{ikm}} (\Phi_h)_t v_h \, d\Omega - \int_{\Omega_{ikm}} g_1 \Phi_h (v_h)_x \, d\Omega - \int_{\Omega_{ikm}} g_3 \Phi_h (v_h)_w \, d\Omega - \int_{\Omega_{ikm}} g_4 \Phi_h (v_h)_\mu \, d\Omega + F_x^+ - F_x^- + F_w^+ - F_w^- + F_\mu^+ - F_\mu^- = \int_{\Omega_{ikm}} C(\Phi_h) v_h \, d\Omega \tag{3.17}$$

for any test function $v_h \in V_h^\ell$. In (3.17),

$$F_x^+ = \int_{w_{k-\frac{1}{2}}}^{w_{k+\frac{1}{2}}} \int_{\mu_{m-\frac{1}{2}}}^{\mu_{m+\frac{1}{2}}} g_1 \check{\Phi} v_h^- \left(x_{i+\frac{1}{2}}, w, \mu\right) dw \, d\mu,$$

$$F_x^- = \int_{w_{k-\frac{1}{2}}}^{w_{k+\frac{1}{2}}} \int_{\mu_{m-\frac{1}{2}}}^{\mu_{m+\frac{1}{2}}} g_1 \check{\Phi} v_h^+ \left(x_{i-\frac{1}{2}}, w, \mu\right) dw \, d\mu,$$

$$F_w^+ = \int_{x_{i-\frac{1}{2}}}^{x_{i+\frac{1}{2}}} \int_{\mu_{m-\frac{1}{2}}}^{\mu_{m+\frac{1}{2}}} g_3 \widehat{\Phi} v_h^- \left(x, w_{k+\frac{1}{2}}, \mu\right) dx \, d\mu,$$

$$F_w^- = \int_{x_{i-\frac{1}{2}}}^{x_{i+\frac{1}{2}}} \int_{\mu_{m-\frac{1}{2}}}^{\mu_{m+\frac{1}{2}}} g_3 \widehat{\Phi} v_h^+ \left(x, w_{k-\frac{1}{2}}, \mu\right) dx \, d\mu,$$

$$F_\mu^+ = \int_{x_{i-\frac{1}{2}}}^{x_{i+\frac{1}{2}}} \int_{w_{k-\frac{1}{2}}}^{w_{k+\frac{1}{2}}} g_4 \widetilde{\Phi} v_h^- \left(x, w, \mu_{m+\frac{1}{2}}\right) dx \, dw,$$

$$F_\mu^- = \int_{x_{i-\frac{1}{2}}}^{x_{i+\frac{1}{2}}} \int_{w_{k-\frac{1}{2}}}^{w_{k+\frac{1}{2}}} g_4 \widetilde{\Phi} v_h^+ \left(x, w, \mu_{m-\frac{1}{2}}\right) dx \, dw,$$

where the upwind numerical fluxes $\check{\Phi}, \widehat{\Phi}, \widetilde{\Phi}$ are chosen according to the following rules:

- The sign of g_1 only depends on μ, if $\mu_m > 0, \check{\Phi} = \Phi^-$; otherwise, $\check{\Phi} = \Phi^+$.
- The sign of g_3 only depends on $\mu E(t,x)$, if $\mu_m E(t, x_i) < 0, \widehat{\Phi} = \Phi^-$; otherwise, $\widehat{\Phi} = \Phi^+$.
- The sign of g_4 only depends on $E(t,x)$, if $E(t, x_i) < 0, \widetilde{\Phi} = \Phi^-$; otherwise, $\widetilde{\Phi} = \Phi^+$.

At the source and drain contacts, we implement the same boundary condition as proposed in [6] to realize neutral charges. In the (w,μ)-space, no boundary condition is necessary, since

- At $w = 0, g_3 = 0$. At $w = w_{\max}$, Φ is machine zero.
- At $\mu = \pm 1, g_4 = 0$,

$F_w^+, F_w^-, F_\mu^+, F_\mu^-$ are always zero. This saves us the effort of constructing ghost elements in comparison with WENO.

The Poisson equation (2.14) is solved by the LDG method on a consistent grid of (3.15) in the x-direction. It involves rewriting the equation into the following form:

$$\begin{cases} q = \frac{\partial \Psi}{\partial x}, \\ \frac{\partial}{\partial x}(\epsilon_r q) = R(t,x), \end{cases} \tag{3.18}$$

where $R(t,x) = c_p[\rho(t,x) - \mathcal{N}_D(x)]$ is a known function that can be computed at each time step once Φ is solved from (3.17), and the coefficient ϵ_r here is a constant. The grid we use is $I_i = \left[x_{i-\frac{1}{2}}, x_{i+\frac{1}{2}}\right]$, with $i = 1, \ldots, N_x$. The approximation space is

$$W_h^\ell = \{v : v|_{I_i} \in P^\ell(I_i)\},$$

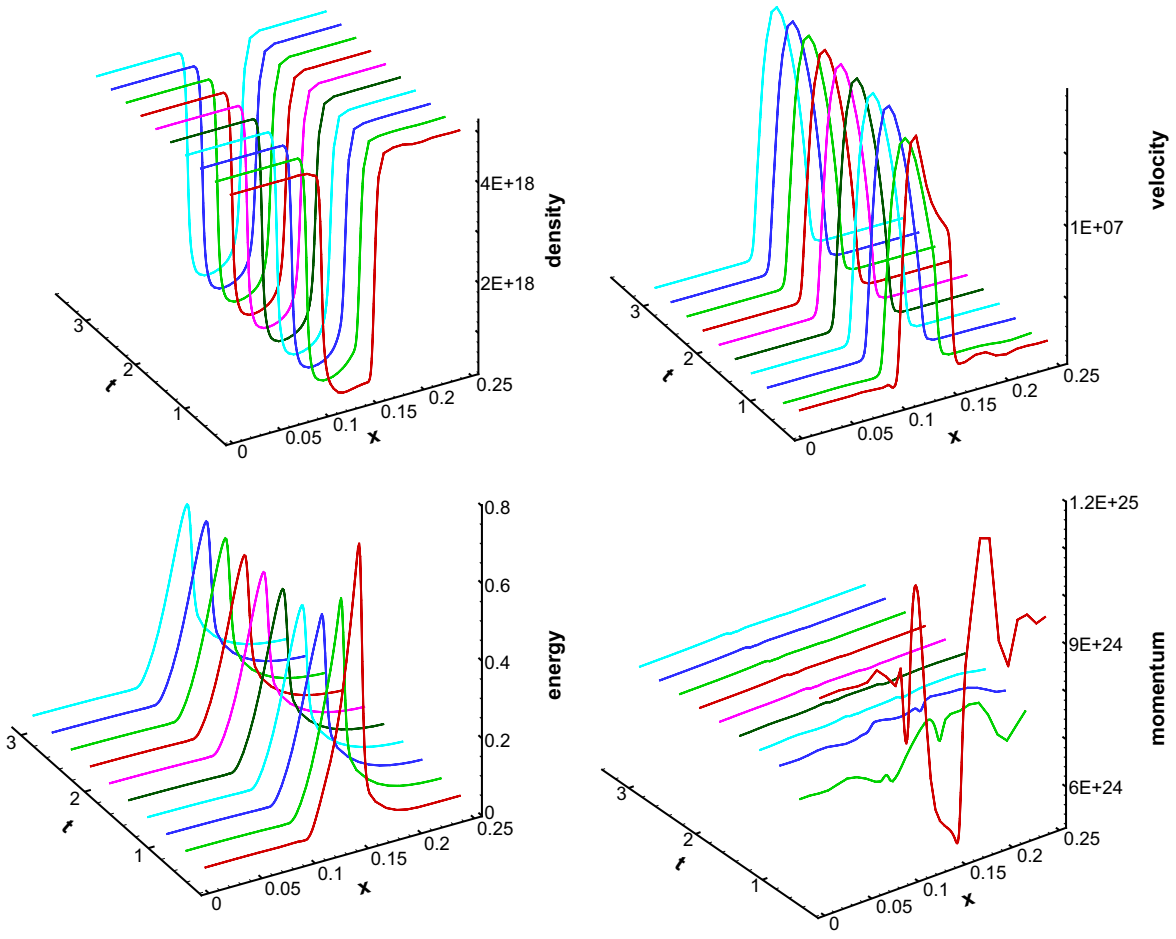

Fig. 3.5. Time evolution of macroscopic quantities using DG method for 50 nm channel at $V_{\text{bias}} = 1.0$ V. Top left: density in cm^{-3}; top right: mean velocity in cm/s; bottom left: energy in eV; bottom right: momentum in $\text{cm}^{-2}\,\text{s}^{-1}$.

with $P^{\ell}(I_i)$ denoting the set of all polynomials of degree at most ℓ on I_i. The LDG scheme for (3.18) is given by: to find $q_h, \Psi_h \in V_h^{\ell}$, such that

$$\int_{I_i} q_h v_h dx + \int_{I_i} \Psi_h (v_h)_x dx - \widehat{\Psi}_h v_h^- \left(x_{i+\frac{1}{2}}\right) + \widehat{\Psi}_h v_h^+ \left(x_{i-\frac{1}{2}}\right) = 0,$$
$$- \int_{I_i} \epsilon_r q_h (p_h)_x dx + \widehat{\epsilon_r q}_h p_h^- \left(x_{i+\frac{1}{2}}\right) - \widehat{\epsilon_r q}_h p_h^+ \left(x_{i-\frac{1}{2}}\right) = \int_{I_i} R(t,x) p_h dx \tag{3.19}$$

hold true for any $v_h, p_h \in W_h^{\ell}$. In the above formulation, the flux is chosen as follows, $\widehat{\Psi}_h = \Psi_h^-, \widehat{\epsilon_r q}_h = \epsilon_r q_h^+ - [\Psi_h]$, where $[\Psi_h] = \Psi_h^+ - \Psi_h^-$. At $x = L$ we need to flip the flux to $\widehat{\Psi}_h = \Psi_h^+, \widehat{\epsilon_r q}_h = \epsilon_r q_h^- - [\Psi_h]$ to adapt to the Dirichlet boundary conditions. Solving (3.19), we can obtain the numerical approximation of the electric potential Ψ_h and electric field $E_h = -c_r q_h$ on each cell I_i.

We include some of the technical details of the implementations for a 2D device in Appendix A. 1D diodes simulation carries similar steps and is simpler. We start with an initial value for Φ_h described in Appendix A.5. The DG-LDG algorithm advances from t^n to t^{n+1} in the following steps:

Step 1: Compute $\rho_h(t,x) = \pi \int_0^{+\infty} dw \int_{-1}^{1} d\mu \Phi_h(t,x,w,\mu)$ as described in Appendix A.6.

Step 2: Use $\rho_h(t,x)$ to solve from (3.19) the electric field, and compute $g_i, i = 1,3,4$ on each computational element.

Step 3: Solve (3.17) and get a method of line ODE for Φ_h, see Appendices A.2, A.3 and A.4.

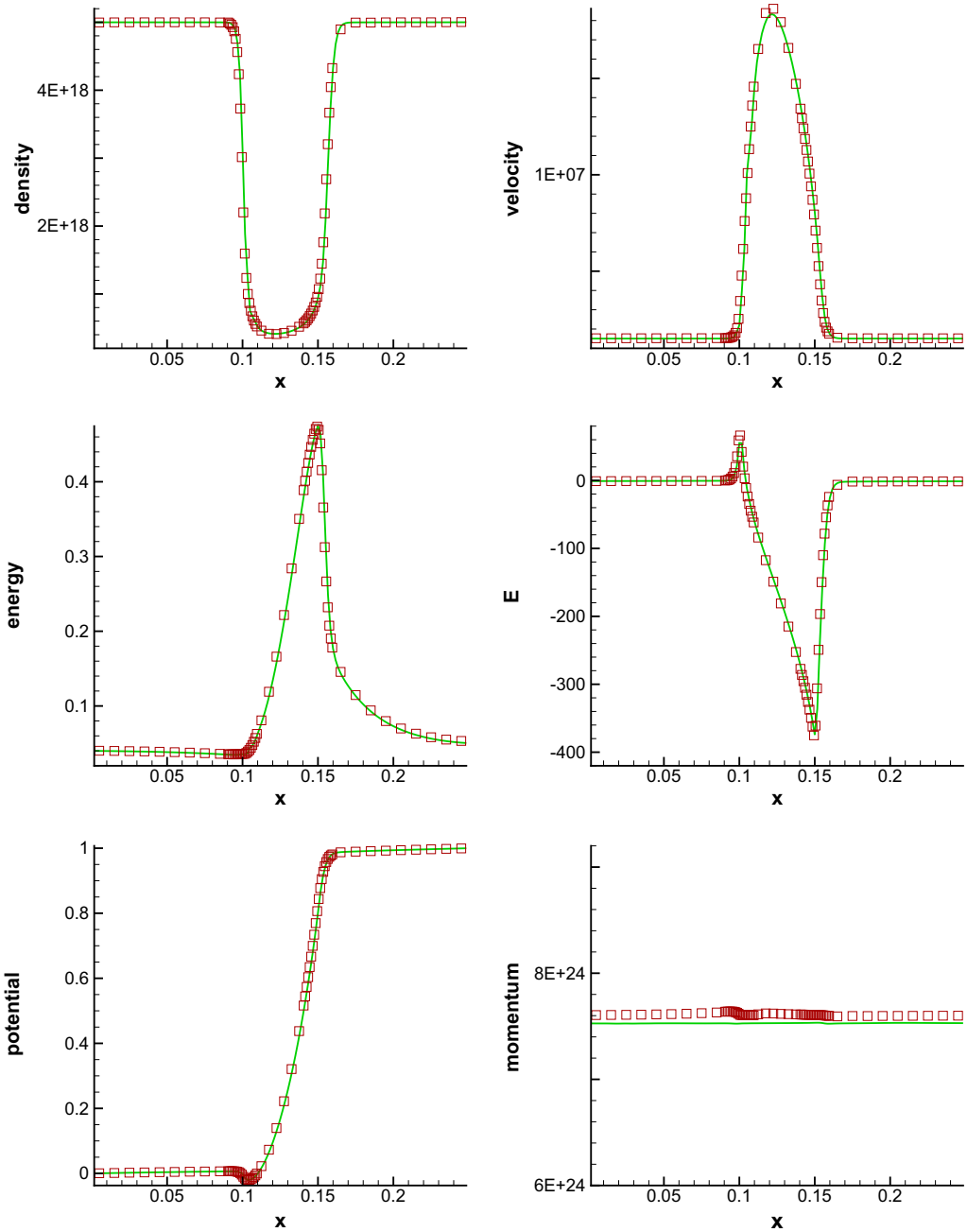

Fig. 3.6. Comparison of macroscopic quantities using DG (symbols) and WENO (solid line) for 50 nm channel at $t = 3.0$ ps, $V_{\text{bias}} = 1.0$ V. Top left: density in cm^{-3}; top right: mean velocity in cm/s; middle left: energy in *eV*; middle right: electric field in kV/cm; bottom left: potential in *V*; bottom right: momentum in cm^{-2} s^{-1}. Solution has reached steady state.

Step 4 Evolve this ODE by proper time stepping from t^n to t^{n+1}, if partial time step is necessary, then repeat Steps 1–3 as needed.

Finally, the hydrodynamic moments can be computed at any time step by the method in Appendix A.6.

We want to remark that, unlike WENO, the DG formulation above has no restriction on the mesh size. In fact, nonuniform meshes are more desirable in practice. For small semiconductor devices with highly doped, non-smooth regions, strong relative electric fields give high energy to charged particles, so it is expected to create states whose distribution functions f have high densities in some regions but low densities in others. Only a nonuniform grid can guarantee accurate results without using a large number of grid points. In particular the evolving distribution function $f(t,x,k)$ has, at some regions points in the physical domain corresponding to strong force fields, a shape that is very different from a Maxwellian distribution (the expected equilibrium statistical state in the absence of electric field), see for example Fig. 3.11. Moreover, taking into account the rapid decay of f for large value of $|\mathbf{k}|$, a nonuniform grid is more computational efficient without sacrificing accuracy of the calculation.

In the following simulations, we have implemented, without self-adaptivity, a nonuniform mesh that refines locally near the regions where most of the interesting phenomena happen, that is the junctions of the channel, addressing one of the main difficulties in solving the Boltzmann–Poisson system with the presence of the doping, which creates strong gradients of the solution near its jumps, and the polar angle direction $\mu = 1$, corresponding to the alignment with the force electric field.

Consequently, for this first computational implementations of the DG solver, using the ansatz that the doping profile function $N_D(x)$ in the Poisson equation does not depend on time, we have the advantage to know where we need a fine grid in space to guarantee a reasonable accuracy.

Even in the simplest test problem of the bulk case, the electric field is constant and the solution is spatially homogeneous. If the initial condition is a Maxwellian distribution function, then, for high constant electric field, one observes the overshoot velocity problem which stabilizes in time. This fact implies that the final

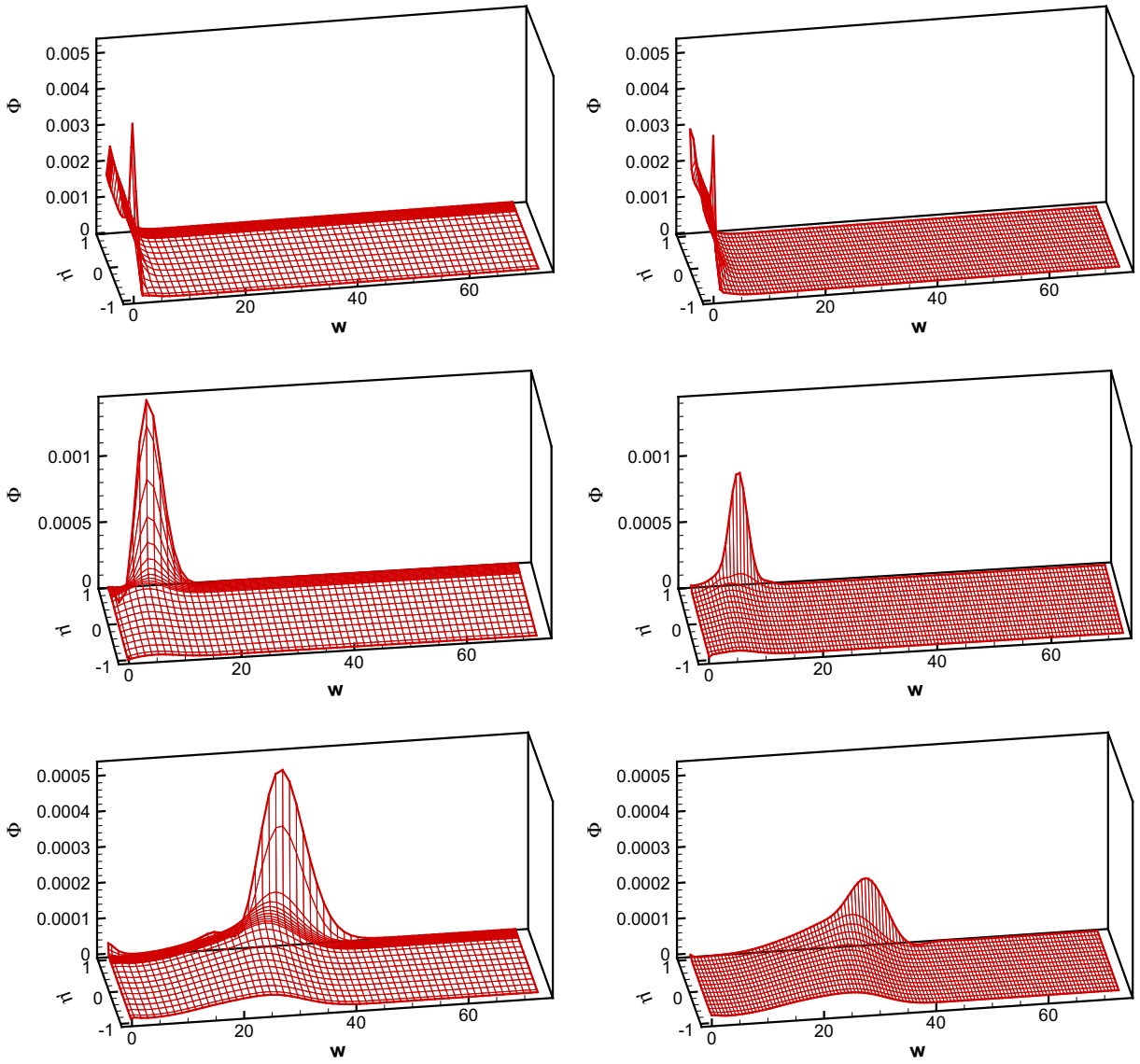

Fig. 3.7. Comparison of the snapshot for $\Phi(x_0, w, \mu)$ using DG (left) and WENO (right) for 50 nm channel at $t = 0.5$ ps, $V_{\text{bias}} = 1.0$ V. Top: $x_0 = 0.1$ μm; middle: $x_0 = 0.125$ μm; bottom: $x_0 = 0.15$ μm. Solution has not yet reached steady state.

state distribution tails change with respect to the initial one, and the distribution has also a shift proportional to the potential energy Φ, therefore a simple choice a fixed mesh in (w,μ) works for a given constant electric field that depends on a potential bias at contacts. In general, due to the stabilization nature of the Boltzmann–Poisson system, the choice of a fixed nonuniform mesh works for this preliminary implementation. However, the magnitude of the gradient variation of the solutions depends on the applied bias, ultimately adaptivity will be the most efficient way to calculate the solution, and so self adaptive DG schemes will be studied in our future work. Nevertheless, we anticipate that a self adaptive scheme has the advantage of a smaller number of cells, but the overhead for the adjustment of the solution to a new grid might be CPU time consuming.

3.2. Discussions on benchmark test problems

We consider two benchmark test examples: Si n^+—n—n^+ diodes of a total length of 1 and 0.25 μm, with 400 and 50 nm channels located in the middle of the device, respectively. For the 400 nm channel device, the dimensional doping is given by $N_D = 5\times 10^{17}$ cm^{-3} in the n^+ region and $N_D = 2\times 10^{15}$ cm^{-3} in the n^- region. For the 50 nm channel device, the dimensional doping is given by $N_D = 5\times 10^{18}$ cm^{-3} in the n^+ region and $N_D = 1\times 10^{15}$ cm^{-3} in the n^- region. Both examples were computed by WENO in [5].

In our simulation, we use piecewise linear polynomials, i.e. $\ell = 1$, and second-order Runge–Kutta time discretization. The doping N_D is smoothed in the following way near the channel junctions to obtain non-oscillatory solutions. Suppose $N_D = N_D^+$ in the n^+ region, $N_D = N_D^-$ in the n^- region and the length of the transition region is 2 cells, then the smoothed function is $(N_D^+ - N_D^-)(1-y^3)^3 + N_D^-$, where $y = (x - x_0 + \Delta x)/(2\Delta x + 10^{-20})$ is the coordinate transformation that makes the transition region $(x_0 - \Delta x, x_0 + \Delta x)$ varies from 0 to 1 in y.

The nonuniform mesh we use for 400 nm channels is defined as follows. In the x-direction, if $x < 0.2$ μm or $x > 0.4$ μm, $\Delta x = 0.01$ μm. In the region 0.2 μm $< x <$ 0.4 μm, $\Delta x = 0.005$ μm. Thus, the total number of cells in x direction is 120. In the w-direction, we use 60 uniform cells. In the μ-direction, we use 24 cells, 12 in the region $\mu < 0.7$, 12 in $\mu > 0.7$. Thus, the grid consists of

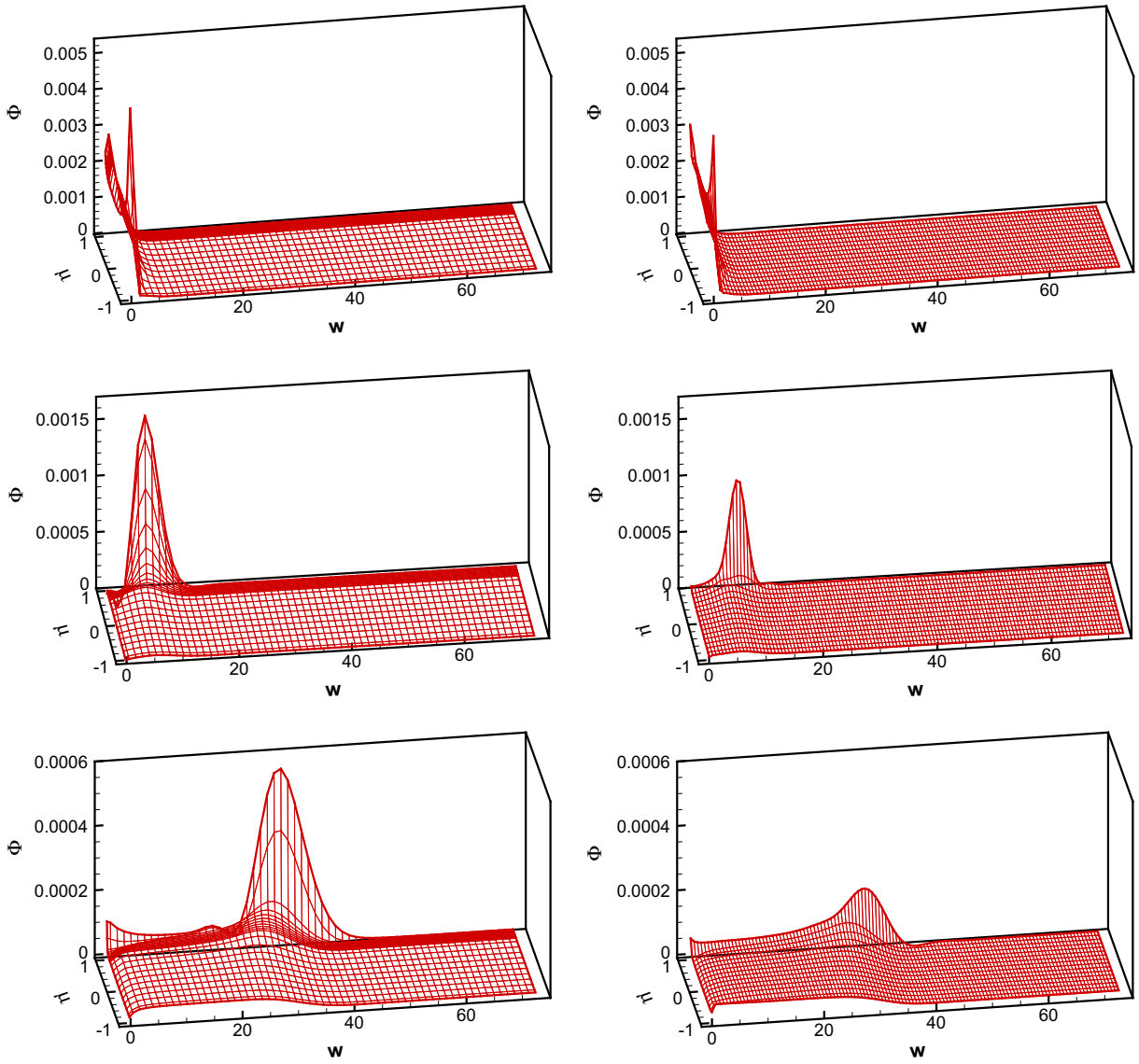

Fig. 3.8. Comparison of the snapshot for $\Phi(x_0, w, \mu)$ using DG (left) and WENO (right) solution for 50 nm channel at $t = 3.0$ ps, $V_{\text{bias}} = 1.0$. Top: $x_0 = 0.1$ μm; middle: $x_0 = 0.125$ μm; bottom: $x_0 = 0.15$ μm. Solution has reached steady state.

$120 \times 60 \times 24$ cells, compared to the WENO grid of $180 \times 60 \times 24$ uniform cells. We should remark that there are more degrees of freedom per cell for DG than for WENO, hence a more adequate comparison is the CPU cost to obtain the same level of errors, see for example [30] in which such a comparison is made for some simple examples indicating the advantage of DG in certain situations.

We plot the evolution of density, mean velocity, energy and momentum in Fig. 3.1. Due to the conservation of mass, which the DG scheme satisfies for our boundary condition, one can see that when the momentum becomes constant, the solution is stable. The solution has already stabilized at $t = 5.0$ ps from the momentum plots. The macroscopic quantities at steady state are plotted in Fig. 3.2. The results are compared with the WENO calculation. They agree with each other in general, with DG offering more resolution and a higher peak in energy near the junctions. This is crucial to obtain a more agreeable kinetic energy with experiments and DSMC simulations. Figs. 3.3 and 3.4 show comparisons for the *pdf* at transient and steady state. We plot at different positions of the device, namely, the left, center and right of the channel. We notice a larger value of *pdf* especially at the center of the channel, where the *pdf* is no longer Maxwellian. Moreover, at $t = 0.5$ ps, $x_0 = 0.5$ μm, the *pdf* shows a double hump structure, which is not captured by the WENO solver. All of these advantages come from the fact that we are refining more near $\mu = 1$. To have a better idea of the shape of the *pdf*, we plot $\Phi(t = 5.0\ \text{ps}, x = 0.5\ \mu\text{m})$ in the cartesian coordinates in Fig. 3.9. The coordinate $V1$ in the plot is the momentum parallel to the force field $k_1, V2$ is the modulus of the orthogonal component. The peak is captured very sharply compared to WENO, see Figs. 3 and 4 in [5].

The nonuniform mesh we use for 50 nm channels is defined as follows. In the x-direction, near the junctions, in $0.09\ \mu\text{m} < x < 0.11\ \mu\text{m}$ and $0.14\ \mu\text{m} < x < 0.16\ \mu\text{m}, \Delta x = 0.001$ μm; in center of the channel $0.11\ \mu\text{m} < x < 0.14\ \mu\text{m}, \Delta x = 0.005$ μm; at everywhere else, $\Delta x = 0.01$ μm. Thus, the total number of cells in x direction is 64. In the w-direction, we use 60 uniform cells. In the μ-direction, we use 20 cells, 10 in the region $\mu < 0.7$, 10 in $\mu > 0.7$. Thus, the grid consists of $64 \times 60 \times 20$ cells, compared to the WENO calculation of $150 \times 120 \times 16$ uniform cells. The evolution and steady state plots are listed in Figs. 3.5–3.7 and 3.8. The conclusions are similar with 400 nm, that we obtain better resolutions near the channel junctions and the peak for *pdf* is much higher. Fig. 3.10 plots $\Phi(t = 5.0\ \text{ps}, x = 0.125\ \mu\text{m})$ in the cartesian coordinates. The peak is twice the height of WENO and is very sharp. Fig. 3.11 plots the *pdf* near $x = 0.15$ μm, the drain junction. We obtain distributions far away from statistical equilibrium, that reflects the lack of suitability of the classical hydrodynamical models for the drain region of a small gated device under even moderate voltage bias.

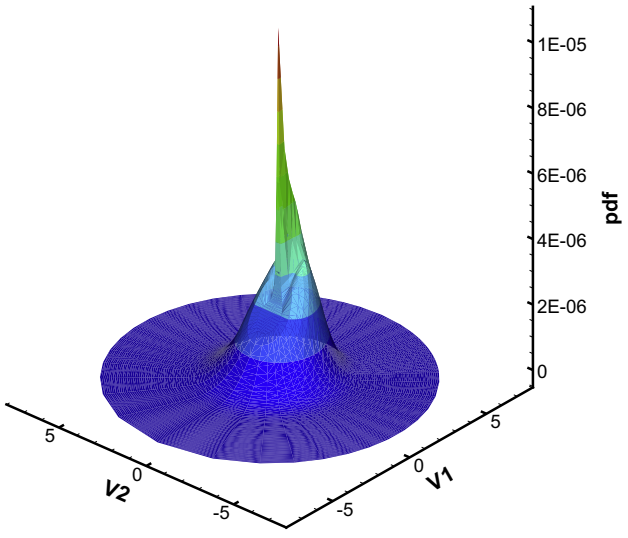

Fig. 3.9. PDF for 400 nm channel at $t = 5.0$ ps, $x = 0.5$ μm. Center of the channel.

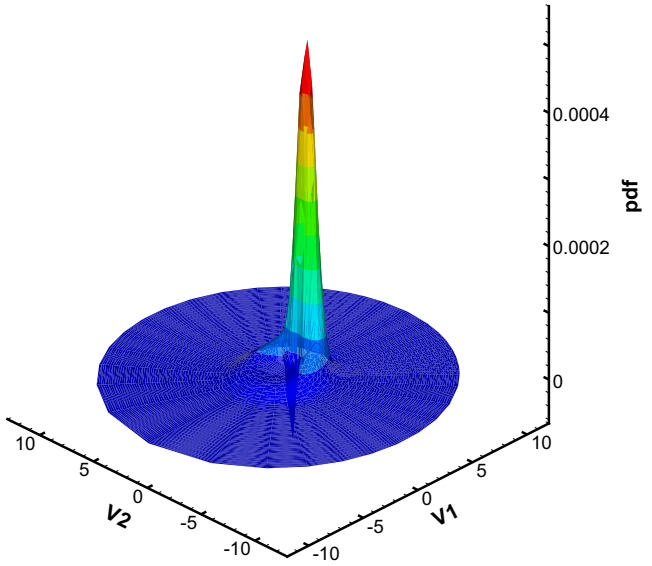

Fig. 3.10. PDF for 50 nm channel at $t = 3.0$ ps, $x = 0.125$ μm. Center of the channel.

3.3. Comparisons with DSMC simulations

We compare the results from DG-BTE solver with those obtained from DSMC simulations (see Figs. 3.12 and 3.13). Both simulations show good agreement except for the kinetic energy near the boundaries.

This mismatch is due to the modeling of the contact boundary conditions in DSMC simulations, which require the knowledge of the distribution function f (or the corresponding energy-band transform Φ) for entering particles. A classical way to solve this problem for DSMC simulations is done by the inclusion of a transport kinetic equation for the dynamic of the electron at the metal junctions. However, this is not realistic due to the complexity of this new kinetic equation, where the importance of electron–electron interaction requires a nonlinear collisional operator, similar to the classical one of the Boltzmann equation for a rarefied perfect gas.

Nevertheless, traditionally, boundary conditions associated with these DSMC models for charge electron transport have been implemented by the following two simplistic rules consisting on the assumption that the distribution function f, near the contact but outside the computational domain is, either proportional to a Maxwellian equilibrium distribution function for incoming velocities, or related to f evaluated near the contact and inside the computational domain. (For strong electric fields near the boundaries, these choices are not correct, as they may required a shift Maxwellian or a condition that generates momentum in the direction of the field.)

The first option is well accepted when a high doping concentration near the boundaries yields a very small electric field: so, the electron gas, in these zones, is almost in the thermal equilibrium and has a constant velocity approximately. That is, we could use the ansatz that the distribution function Φ, in the outer side of the boundary is taken to be proportional to a energy-band spherically transformed Maxwellian equilibrium distribution function

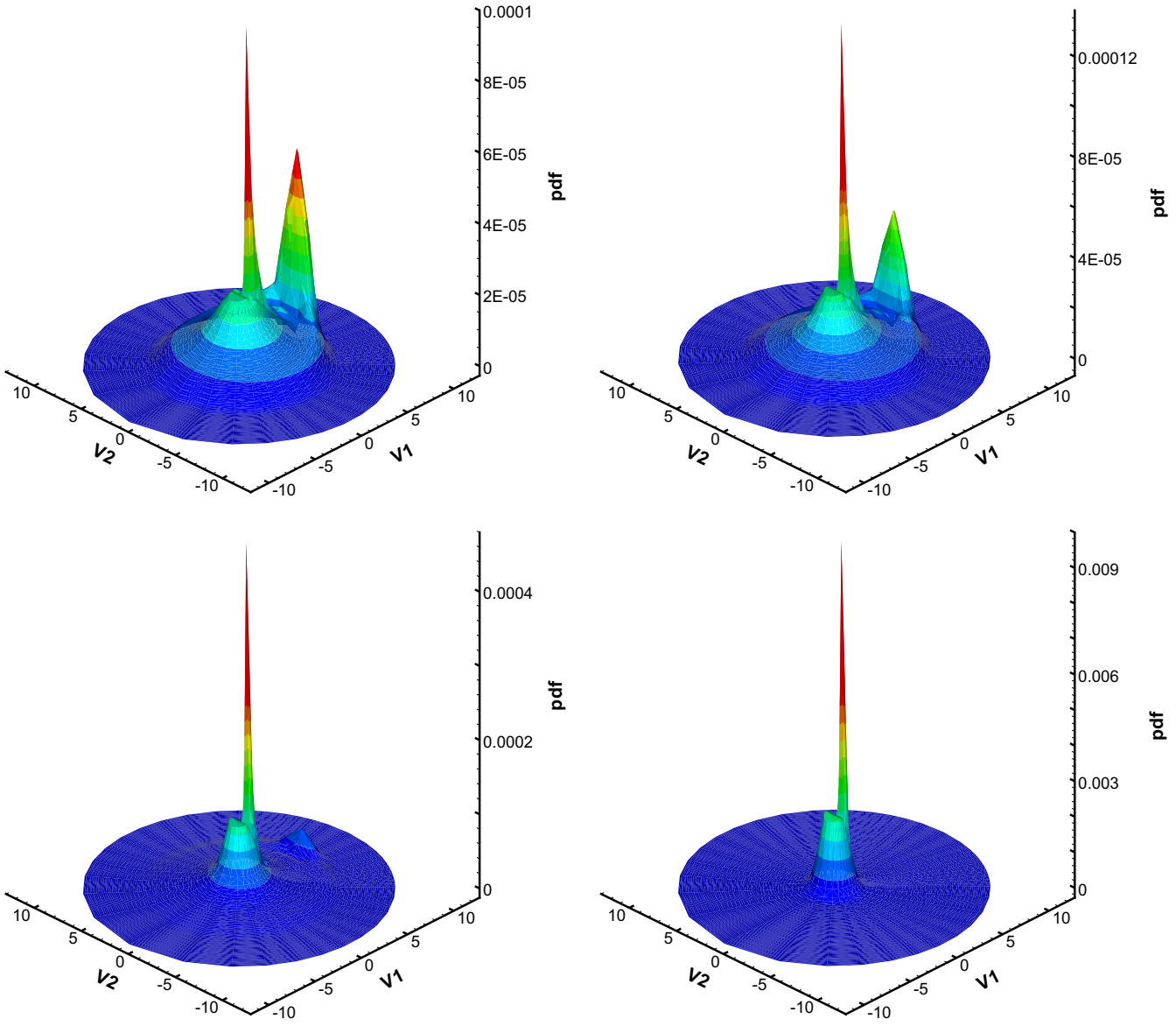

Fig. 3.11. Non-equilibrium PDF states near the drain junction for 50 nm channel at $t = 3.0$ ps. They exhibit the large deviation from classical statistical states even at places corresponding to highly doped region. This is a signature of hot electron transport. Top left: $x = 0.149$ μm. Top right: $x = 0.15$ μm. Bottom left: $x = 0.152$ μm. Bottom right: $x = 0.16$ μm.

centered at zero energy, whose average matches the doping profile function $N_D(\mathbf{x})$ at the boundary. However this approach will create boundary layers of the mean free path order and so the condition do not secure an absolute charge neutrality.

Hence, we rather use the second option which imposes that $f = f_{out}$, near the contact and outside the computational domain $(k \cdot \eta_{x_b} < 0)$ where x_b is a boundary point and η_{x_b} the outer normal, is related to $f = f_{in}$ evaluated near the contact and inside the computational domain $(k \cdot \eta_{x_b} > 0)$. This approach allows us to get an exact *neutral charge* at the source and drain contact boundaries, which imposes that the probability and doping density must coincide, as well as continuity in velocity space. Then the simple formula,

$$\Phi_{out}(t, x_b, w, \mu) = \frac{\mathcal{N}_D(x_b)}{\rho(t, x_b)} \Phi_{in}(t, x_b, w, \mu) \tag{3.20}$$

is assumed in our simulations, where Φ_{out} is the band-energy spherically coordinated transformed f_{out}, in the corresponding transform domain.

This very same boundary type condition (3.20) at the gate and drain contacts has been used in the deterministic simulations of Boltzmann–Poisson systems for semiconductor devices by WENO schemes (see [6]) and are use here for the DG schemes to approximate the same boundary value problem. So the agreement of lower moments is very good, even though at the computational level, (3.20) is approximated in different ways depending on the numerical scheme.

For example, in the case of DSMC simulations, particles must be created or destroyed. However in the case of finite difference WENO schemes, we introduced suitable ghost points [4,6]; and in the case of DG schemes it is enough to give values of Φ at boundaries according to condition (3.20).

Hence, we can not have a unique exact boundary conditions in the computational experiments, which makes it clear that these differences in the numerical boundary treatment have an influence for the solutions at the stationary regime, which explains the discrepancies of the numerical comparisons of moments near the boundaries. Nevertheless, we stress that, as Figs. 3.5 and 3.6 show

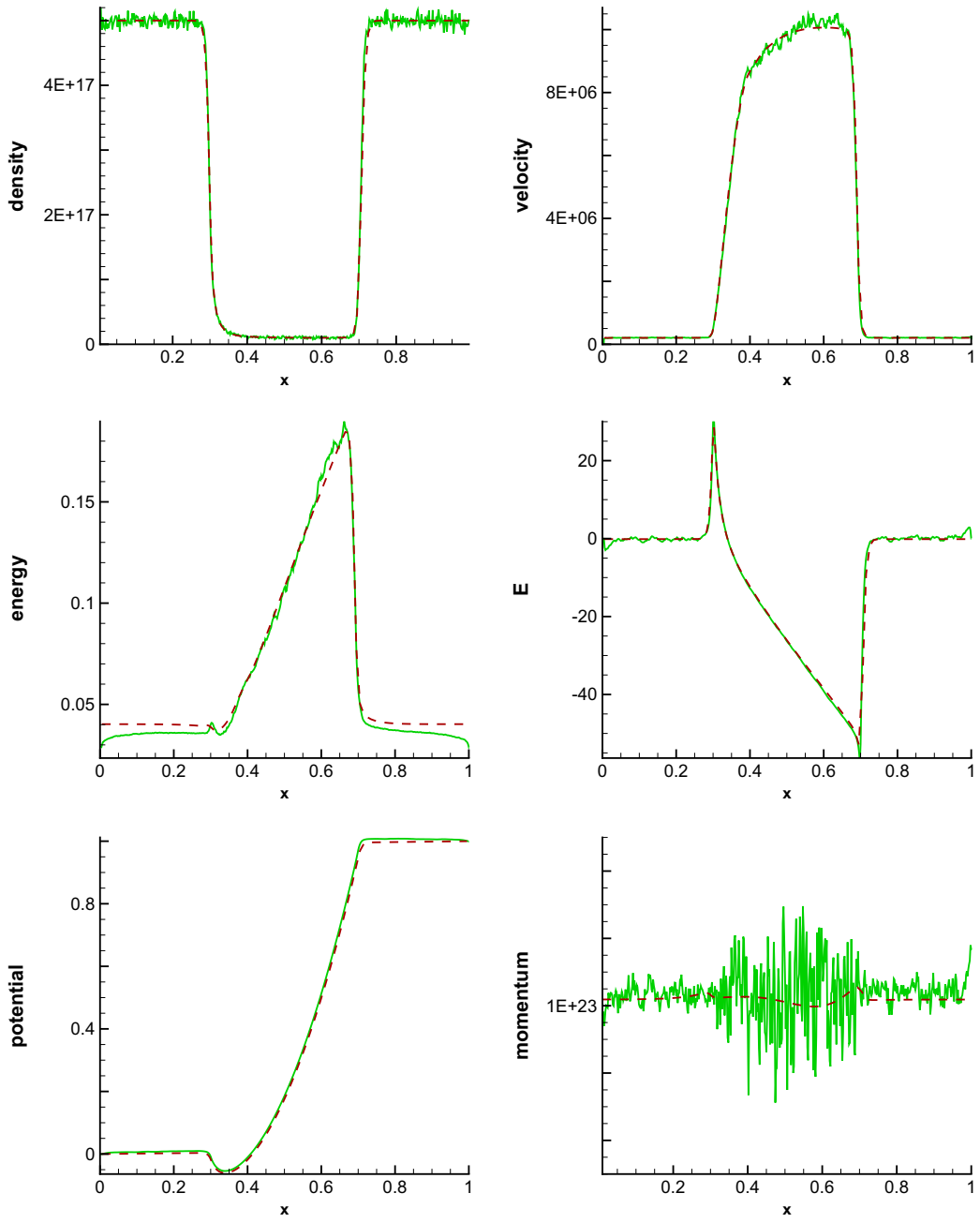

Fig. 3.12. Comparison of macroscopic quantities using DG (dashed line) and DSMC (solid line) for 400 nm channel at $t = 5.0$ ps, $V_{\text{bias}} = 1.0$ V. Top left: density in cm^{-3}; top right: mean velocity in cm/s; middle left: energy in eV; middle right: electric field in kV/cm; bottom left: potential in V; bottom right: momentum in $\text{cm}^{-2}\ \text{s}^{-1}$. Solution has reached steady state.

in all cases, there is a very good agreement of the comparisons inside the device.

3.4. Summary

We have benchmarked the DG algorithm on two test cases: Si n^+—n—n^+ diodes with 400 and 50 nm channels. The DG scheme has the ability to quickly stabilize to the steady state and accurately resolve transient details. In particular, the *pdf* along the direction of the electric field is captured sharply due to the nonuniform mesh we use. For the more energetic device with 50 nm channel, DG computes a much higher peak and a "donut" shaped tail in the *pdf* near the drain junction, thus resulting in an accurate description of higher order moments in those regions.

4. DG-BTE solver for 2D double gate MOSFET simulation

In this section, we turn to a 2D double gate MOSFET device. The algorithm is similar to those described in the previous section. For the benefit of the reader, we repeat some of the procedures in Section 3. We will use a simple rectangular grid and let

$$\Omega_{ijkmn} = \left[x_{i-\frac{1}{2}}, x_{i+\frac{1}{2}}\right] \times \left[y_{j-\frac{1}{2}}, y_{j+\frac{1}{2}}\right] \times \left[w_{k-\frac{1}{2}}, w_{k+\frac{1}{2}}\right] \times \left[\mu_{m-\frac{1}{2}}, \mu_{m+\frac{1}{2}}\right] \times \left[\varphi_{n-\frac{1}{2}}, \varphi_{n+\frac{1}{2}}\right],$$

where
$i = 1, \ldots N_x,\ j = 1, \ldots N_y,\ k = 1, \ldots N_w,\ m = 1, \ldots N_\mu,\ n = 1, \ldots N_\varphi$,
and

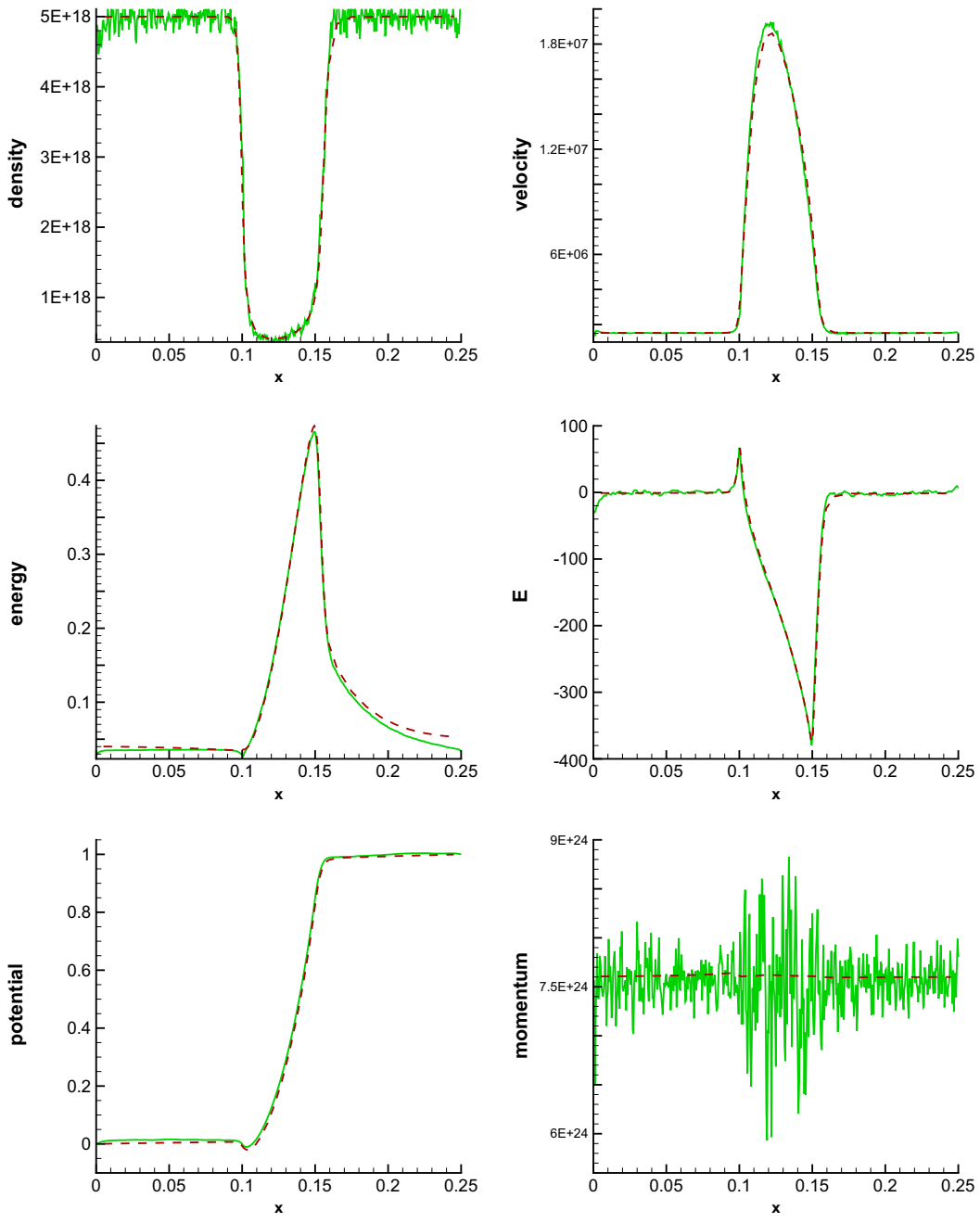

Fig. 3.13. Comparison of macroscopic quantities using DG (dashed line) and DSMC (solid line) for 50 nm channel at $t = 3.0$ ps, $V_{\text{bias}} = 1.0\,V$. Top left: density in cm^{-3}; top right: mean velocity in cm/s; middle left: energy in eV; middle right: electric field in kV/cm; bottom left: potential in V; bottom right: momentum in cm^{-2} s^{-1}. Solution has reached steady state.

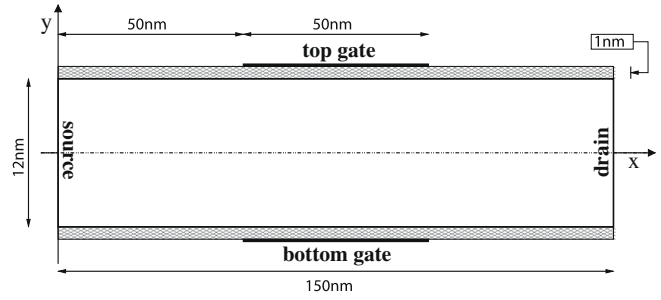

Fig. 4.14. Schematic representation of a 2D double gate MOSFET device.

$$x_{i\pm\frac{1}{2}} = x_i \pm \frac{\Delta x_i}{2}, \quad y_{j\pm\frac{1}{2}} = y_j \pm \frac{\Delta y_j}{2}, \quad w_{k\pm\frac{1}{2}} = w_k \pm \frac{\Delta w_k}{2},$$
$$\mu_{m\pm\frac{1}{2}} = \mu_m \pm \frac{\Delta \mu_m}{2}, \quad \varphi_{n\pm\frac{1}{2}} = \varphi_n \pm \frac{\Delta \varphi_n}{2}.$$

The approximation space is defined as

$$V_h^\ell = \{v : v|_{\Omega_{ijkmn}} \in P^\ell(\Omega_{ijkmn})\}. \tag{4.21}$$

Here, $P^\ell(\Omega_{ijkmn})$ is the set of all polynomials of degree at most ℓ on Ω_{ijkmn}. The DG formulation for the Boltzmann equation (2.9) would be: to find $\Phi_h \in V_h^\ell$, such that

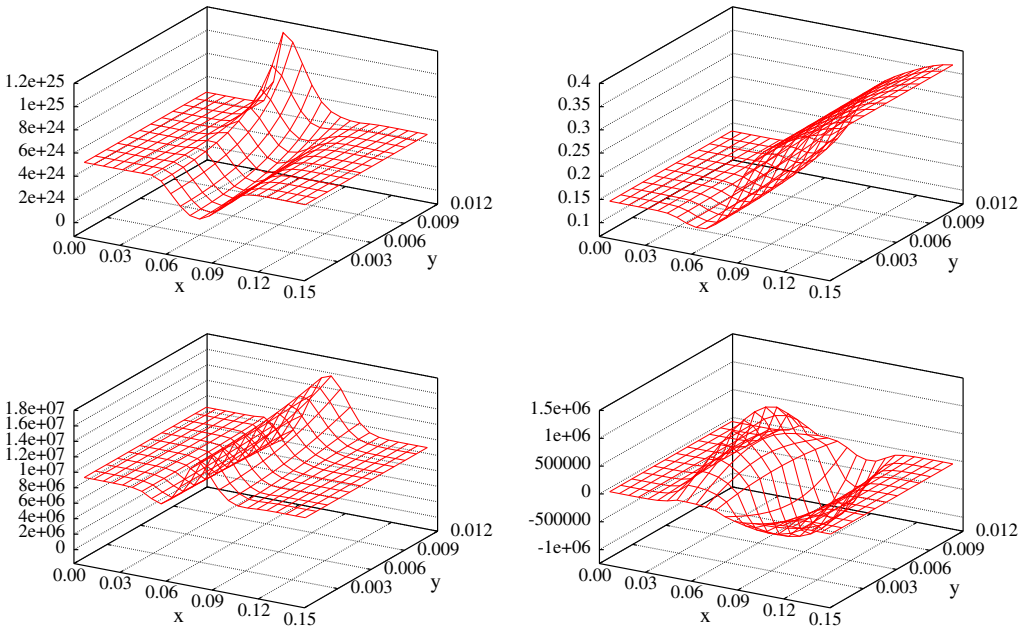

Fig. 4.15. Macroscopic quantities of double gate MOSFET device at $t = 0.5$ ps. Top left: density in cm^{-3}; top right: energy in eV; bottom left: x-component of velocity in cm/s; bottom right: y-component of velocity in cm/s. Solution reached steady state.

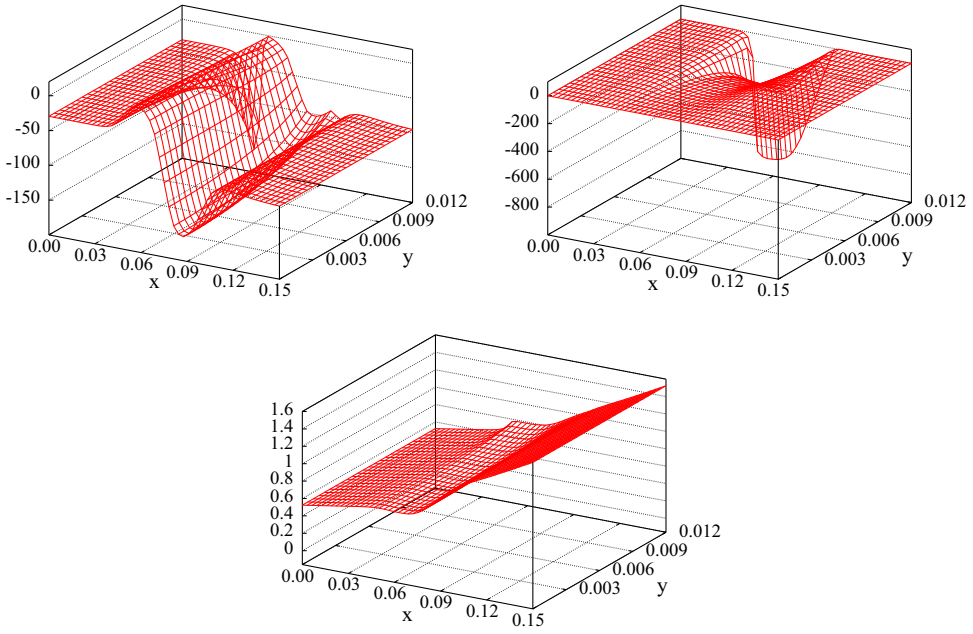

Fig. 4.16. Macroscopic quantities of double gate MOSFET device at $t = 0.5$ ps. Top left: x-component of electric field in kV/cm; top right: y-component of electric field in kV/cm; bottom: electric potential in V. Solution has reached steady state.

$$\int_{\Omega_{ijkmn}} (\Phi_h)_t v_h \, d\Omega - \int_{\Omega_{ijkmn}} g_1 \Phi_h (v_h)_x \, d\Omega - \int_{\Omega_{ijkmn}} g_2 \Phi_h (v_h)_y \, d\Omega$$
$$- \int_{\Omega_{ijkmn}} g_3 \Phi_h (v_h)_w \, d\Omega - \int_{\Omega_{ijkmn}} g_4 \Phi_h (v_h)_\mu \, d\Omega$$
$$- \int_{\Omega_{ijkmn}} g_5 \Phi_h (v_h)_\varphi \, d\Omega + F_x^+ - F_x^- + F_y^+ - F_y^- + F_w^+ - F_w^-$$
$$+ F_\mu^+ - F_\mu^- + F_\varphi^+ - F_\varphi^- = \int_{\Omega_{ijkmn}} C(\Phi_h) v_h \, d\Omega \qquad (4.22)$$

for any test function $v_h \in V_h^\ell$. In (4.22),

$$F_x^\pm = \int_{y_{j-\frac{1}{2}}}^{y_{j+\frac{1}{2}}} \int_{w_{k-\frac{1}{2}}}^{w_{k+\frac{1}{2}}} \int_{\mu_{m-\frac{1}{2}}}^{\mu_{m+\frac{1}{2}}} \int_{\varphi_{n-\frac{1}{2}}}^{\varphi_{n+\frac{1}{2}}} g_1 \check{\Phi} v_h^\mp \left(x_{i\pm\frac{1}{2}}, y, w, \mu, \varphi\right) dy \, dw \, d\mu \, d\varphi,$$

$$F_y^\pm = \int_{x_{i-\frac{1}{2}}}^{x_{i+\frac{1}{2}}} \int_{w_{k-\frac{1}{2}}}^{w_{k+\frac{1}{2}}} \int_{\mu_{m-\frac{1}{2}}}^{\mu_{m+\frac{1}{2}}} \int_{\varphi_{n-\frac{1}{2}}}^{\varphi_{n+\frac{1}{2}}} g_2 \overline{\Phi} v_h^\mp \left(x, y_{j\pm\frac{1}{2}}, w, \mu, \varphi\right) dx \, dw \, d\mu \, d\varphi,$$

$$F_w^\pm = \int_{x_{i-\frac{1}{2}}}^{x_{i+\frac{1}{2}}} \int_{y_{j-\frac{1}{2}}}^{y_{j+\frac{1}{2}}} \int_{\mu_{m-\frac{1}{2}}}^{\mu_{m+\frac{1}{2}}} \int_{\varphi_{n-\frac{1}{2}}}^{\varphi_{n+\frac{1}{2}}} \widehat{g_3 \Phi} v_h^\mp \left(x, y, w_{k\pm\frac{1}{2}}, \mu, \varphi\right) dx \, dy \, d\mu \, d\varphi,$$

$$F_{\mu}^{\pm}=\int_{x_{i-\frac{1}{2}}}^{x_{i+\frac{1}{2}}}\int_{y_{j-\frac{1}{2}}}^{y_{j+\frac{1}{2}}}\int_{w_{k-\frac{1}{2}}}^{w_{k+\frac{1}{2}}}\int_{\varphi_{n-\frac{1}{2}}}^{\varphi_{n+\frac{1}{2}}}\widetilde{g_4\Phi}\,v_h^{\mp}\left(x,y,w,\mu_{m\pm\frac{1}{2}},\varphi\right)dx\,dy\,dw\,d\varphi,$$

$$F_{\varphi}^{\pm}=\int_{x_{i-\frac{1}{2}}}^{x_{i+\frac{1}{2}}}\int_{y_{j-\frac{1}{2}}}^{y_{j+\frac{1}{2}}}\int_{w_{k-\frac{1}{2}}}^{w_{k+\frac{1}{2}}}\int_{\mu_{m-\frac{1}{2}}}^{\mu_{m+\frac{1}{2}}}g_5\dot{\Phi}\,v_h^{\mp}\left(x,y,w,\mu,\varphi_{n\pm\frac{1}{2}}\right)dx\,dy\,dw\,d\mu,$$

where the upwind numerical fluxes $\check{\Phi},\overline{\Phi},\widehat{g_3\Phi},\widetilde{g_4\Phi},\dot{\Phi}$ are defined in the following way:

- The sign of g_1 only depends on μ, if $\mu_m>0$, then $\check{\Phi}=\Phi^-$; otherwise, $\check{\Phi}=\Phi^+$.
- The sign of g_2 only depends on $\cos\varphi$, if $\cos\varphi_n>0$, then $\overline{\Phi}=\Phi^-$; otherwise, $\overline{\Phi}=\Phi^+$. Note that in our simulation, N_φ is always even.
- For $\widehat{g_3\Phi}$, we let

$$\widehat{g_3\Phi}=-2c_k\frac{\sqrt{w(1+\alpha_K w)}}{1+2\alpha_K w}\left[\mu E_x(t,x,y)\widehat{\Phi}+\sqrt{1-\mu^2}\cos\varphi E_y(t,x,y)\widetilde{\Phi}\right].$$

  If $\mu_m E_x(t,x_i,y_j)<0$, then $\widehat{\Phi}=\Phi^-$; otherwise, $\widehat{\Phi}=\Phi^+$.If $(\cos\varphi_n)E_y(t,x_i,y_j)<0$, then $\tilde{\Phi}=\Phi^-$; otherwise, $\tilde{\Phi}=\Phi^+$.

- For $\widetilde{g_4\Phi}$, we let

$$\widetilde{g_4\Phi}=-c_k\frac{\sqrt{1-\mu^2}}{\sqrt{w(1+\alpha_K w)}}\left[\sqrt{1-\mu^2}E_x(t,x,y)\widehat{\Phi}-\mu\cos\varphi E_y(t,x,y)\widetilde{\Phi}\right],$$

  If $E_x(t,x_i,y_j)<0$, then $\widehat{\Phi}=\Phi^-$; otherwise, $\widehat{\Phi}=\Phi^+$.If $\mu_m\cos(\varphi_n)E_y(t,x_i,y_j)>0$, then $\widetilde{\Phi}=\Phi^-$; otherwise, $\widetilde{\Phi}=\Phi^+$.

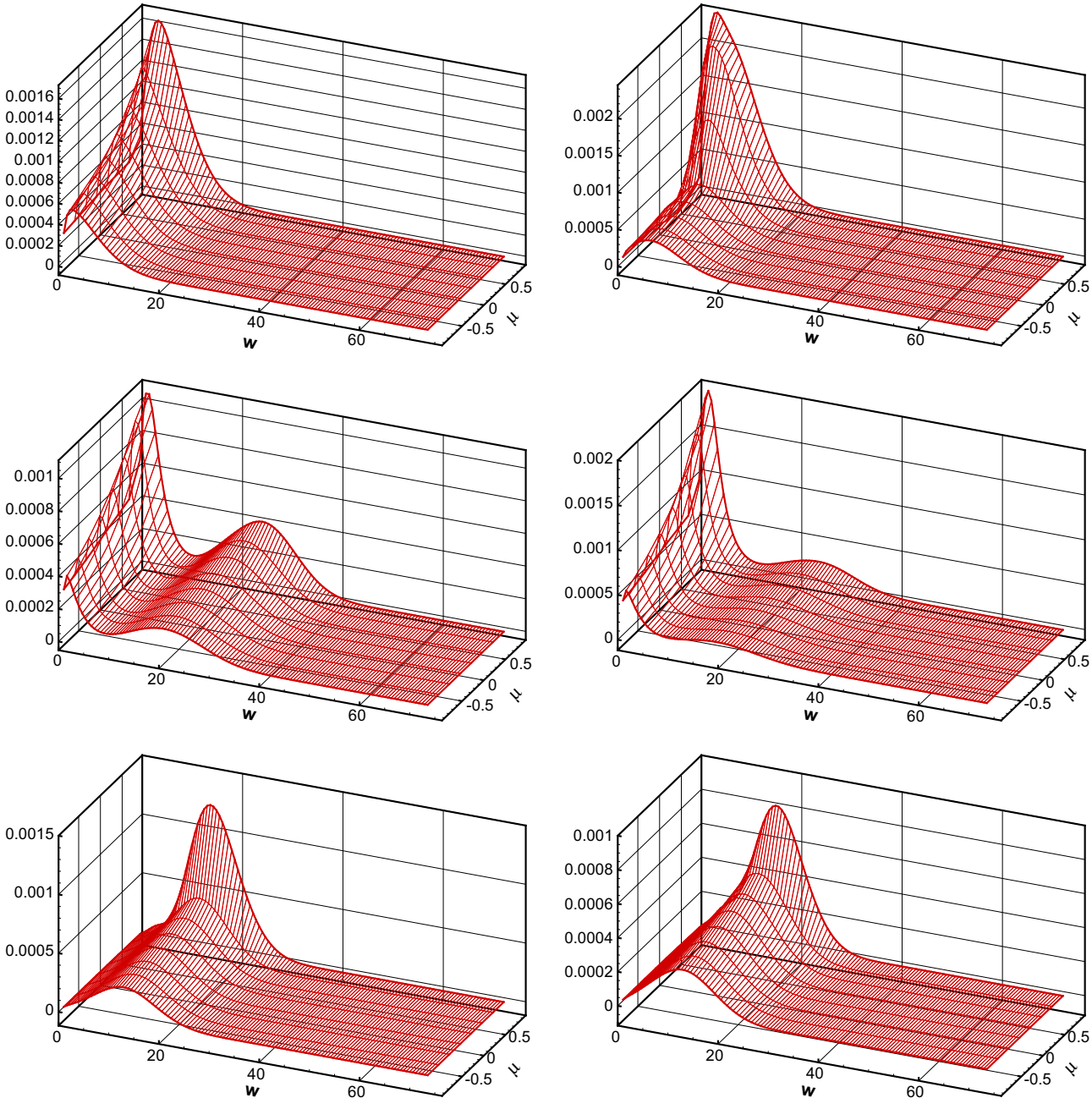

Fig. 4.17. PDF of double gate MOSFET device at $t=0.5$ ps. Top left: at (0.025 μm,0.012 μm); top right: at (0.075 μm,0.012 μm); middle left: at (0.125 μm,0.012 μm); middle right: at (0.1375 μm,0.006 μm); bottom left: at (0.09375 μm, 0.010 μm); bottom right: at (0.09375 μm,0 μm). Solution reached steady state.

- The sign of g_5 only depends on $E_y(t,x,y)$, if $E_y(t,x_i,y_j)>0$, then $\dot{\Phi}=\Phi^-$; otherwise, $\dot{\Phi}=\Phi^+$.

The schematic plot of the double gate MOSFET device is given in Fig. 4.14. The shadowed region denotes the oxide-silicon region, whereas the rest is the silicon region. Since the problem is symmetric about the x-axis, we will only need to compute for $y>0$. At the source and drain contacts, we implement the same boundary condition as proposed in [6] to realize neutral charges. A buffer layer of ghost points of $i=0$ and $i=N_x+1$ is used to make

$$\Phi(i=0)=\Phi(i=1)\frac{N_D(i=1)}{\rho(i=1)},$$

and

$$\Phi(i=N_x+1)=\Phi(i=N_x)\frac{N_D(i=N_x)}{\rho(i=N_x)}.$$

At the top and bottom of the computational domain (the silicon region), we impose the classical elastic specular boundary reflection.

In the (w,μ,φ)-space, no boundary condition is necessary because of similar reason as in the 1D case,

- at $w=0, g_3=0$. At $w=w_{\max}, \Phi$ is machine zero;
- at $\mu=\pm1, g_4=0$;
- at $\varphi=0,\pi, g_5=0$,

so at those boundaries, the numerical flux always vanishes, hence no ghost point is necessary.

For the boundary condition of the Poisson equation, $\Psi=0.52354$ at source, $\Psi=1.5235$ at drain and $\Psi=1.06$ at gate. For the rest of boundaries, we impose homogeneous Neumann boundary condition, i.e., $\frac{\partial\Psi}{\partial n}=0$. The relative dielectric constant in the oxide-silicon region is $\epsilon_r=3.9$, in the silicon region is $\epsilon_r=11.7$.

The Poisson equation (2.11) is solved by the LDG method. It involves rewriting the equation into the following form:

$$\begin{cases} q=\frac{\partial\Psi}{\partial x}, \quad s=\frac{\partial\Psi}{\partial y}, \\ \frac{\partial}{\partial x}(\epsilon_r q)+\frac{\partial}{\partial y}(\epsilon_r s)=R(t,x,y), \end{cases} \tag{4.23}$$

where $R(t,x,y)=c_p[\rho(t,x,y)-\mathcal{N}_D(x,y)]$ is a known function that can be computed at each time step once Φ is solved from (4.22), and the coefficient ϵ_r depends on x,y. The Poisson system is only on the (x,y) domain. Hence, we use the grid $I_{ij}=\left[x_{i-\frac12},x_{i+\frac12}\right]\times\left[y_{j-\frac12},y_{j+\frac12}\right]$, with $i=1,\dots,N_x, j=1,\dots,N_y+M_y$, where $j=N_y+1,\dots,N_y+M_y$ denotes the oxide-silicon region, and the grid in $j=1,\dots,N_y$ is consistent with the five-dimensional rectangular grid for the Boltzmann equation in the silicon region. The approximation space is defined as

$$W_h^\ell=\{v: v|_{I_{ij}}\in P^\ell(I_{ij})\}. \tag{4.24}$$

Here $P^\ell(I_{ij})$ denotes the set of all polynomials of degree at most ℓ on I_{ij}. The LDG scheme for (4.23) is: to find $q_h,s_h,\Psi_h\in V_h^\ell$, such that

$$\begin{aligned}
&\int_{I_{ij}} q_h v_h\,dx\,dy+\int_{I_{ij}}\Psi_h(v_h)_x\,dx\,dy-\int_{y_{j-\frac12}}^{y_{j+\frac12}}\widehat{\Psi}_h v_h^-\left(x_{i+\frac12},y\right)dy\\
&\quad+\int_{y_{j-\frac12}}^{y_{j+\frac12}}\widehat{\Psi}_h v_h^+\left(x_{i-\frac12},y\right)dy=0,\\
&\int_{I_{ij}} s_h w_h\,dx\,dy+\int_{I_{ij}}\Psi_h(w_h)_y\,dx\,dy-\int_{x_{i-\frac12}}^{x_{i+\frac12}}\widetilde{\Psi}_h w_h^-\left(x,y_{j+\frac12}\right)dx\\
&\quad+\int_{x_{i-\frac12}}^{x_{i+\frac12}}\widetilde{\Psi}_h w_h^+\left(x,y_{j-\frac12}\right)dx=0,
\end{aligned}$$

$$\begin{aligned}
&-\int_{I_{ij}}\epsilon_r q_h(p_h)_x\,dx\,dy+\int_{y_{j-\frac12}}^{y_{j+\frac12}}\widehat{\epsilon_r q}_h p_h^-\left(x_{i+\frac12},y\right)dy\\
&-\int_{y_{j-\frac12}}^{y_{j+\frac12}}\widehat{\epsilon_r q}_h p_h^+\left(x_{i-\frac12},y\right)dy-\int_{I_{ij}}\epsilon_r s_h(p_h)_y\,dx\,dy\\
&+\int_{x_{i-\frac12}}^{x_{i+\frac12}}\widetilde{\epsilon_r s}_h p_h^-\left(x,y_{j+\frac12}\right)dx-\int_{x_{i-\frac12}}^{x_{i+\frac12}}\widetilde{\epsilon_r s}_h p_h^+\left(x,y_{j-\frac12}\right)dx\\
&=\int_{I_{ij}} R(t,x,y)p_h\,dx\,dy
\end{aligned}$$

hold true for any $v_h,w_h,p_h\in W_h^\ell$. In the above formulation, we choose the flux as follows, in the x-direction, we use $\widehat{\Psi}_h=\Psi_h^-, \widehat{\epsilon_r q}_h=\epsilon_r q_h^+-[\Psi_h]$. In the y-direction, we use $\widetilde{\Psi}_h=\Psi_h^-, \widetilde{\epsilon_r s}_h=\epsilon_r s_h^+-[\Psi_h]$. On some part of the domain boundary, the above flux needs to be changed to accommodate various boundary conditions [12]. Near the drain, we are given Dirichlet boundary condition, so we need to flip the flux in x-direction: let $\widehat{\Psi}_h\left(x_{i+\frac12},y\right)=\Psi_h^+\left(x_{i+\frac12},y\right)$ and $\widehat{\epsilon_r q}_h\left(x_{i+\frac12},y\right)=\epsilon_r q_h^-\left(x_{i+\frac12},y\right)-[\Psi_h]\left(x_{i+\frac12},y\right)$, if the point $\left(x_{i+\frac12},y\right)$ is at the drain. For the gate, we need to flip the flux in y-direction: let $\widetilde{\Psi}_h\left(x,y_{j+\frac12}\right)=\Psi_h^+\left(x,y_{j+\frac12}\right)$ and $\widetilde{\epsilon_r s}_h\left(x,y_{j+\frac12}\right)=\epsilon_r s_h^-\left(x,y_{j+\frac12}\right)-[\Psi_h]\left(x,y_{j+\frac12}\right)$, if the point $\left(x,y_{j+\frac12}\right)$ is at the gate. For the bottom, we need to use the Neumann condition, and flip the flux in y-direction, i.e., $\widetilde{\Psi}_h=\Psi_h^+, \widetilde{\epsilon_r s}_h=\epsilon_r s_h^-$. This scheme described above will enforce the continuity of Ψ and $\epsilon_r\frac{\partial\Psi}{\partial n}$ across the interface of silicon and oxide-silicon interface. The solution of (4.25) gives us approximations to both the potential Ψ_h and the electric field $(E_x)_h=-c_v q_h$, $(E_y)_h=-c_v s_h$.

To summarize, start with an initial condition for Φ_h (Appendix A.5), the DG-LDG algorithm for the 2D double gate MOSFET advances from t^n to t^{n+1} in the following steps similar to the 1D diodes simulation:

Step 1: Compute $\rho_h(t,x,y)=\int_0^{+\infty}dw\int_{-1}^{1}d\mu\int_0^{\pi}d\varphi\Phi_h(t,x,y,w,\mu,\varphi)$ as described in Appendix A.6.

Step 2: Use $\rho_h(t,x,y)$ to solve from (4.25) the electric field $(E_x)_h$ and $(E_y)_h$, and compute $g_i, i=1,\dots,5$.

Step 3: Solve (4.22) and get a method of line ODE for Φ_h, see Appendices A.2, A.3 and A.4.

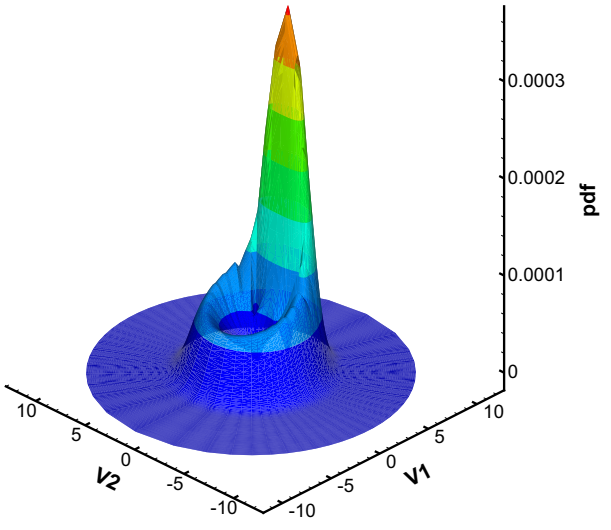

Fig. 4.18. PDF for 2D double gate MOSFET at $t=0.5$ ps, $(x,y)=(0.9375\ \mu m, 0.10\ \mu m)$.

Step 4: Evolve this ODE by proper time stepping from t^n to t^{n+1}, if partial time step is necessary, then repeat Steps 1–3 as needed.

Finally, the hydrodynamic moments can be computed at any time step by the method in Appendix A.6.

All numerical results are obtained with a piecewise linear approximation space and first order Euler time stepping. The dissipative nature of the collision term makes the Euler forward time stepping stable. We use a 24×14 grid in space, 120 points in w, 8 points in μ and 6 points in φ. In Figs. 4.15 and 4.16, we show the results of the macroscopic quantities. We also show the *pdf* at six different locations in the device in Fig. 4.17. These *pdf*'s have been computed by averaging the values of Φ_h over φ. In Fig. 4.18, we present the cartesian plot for *pdf* at $(x,y) = (0.125\ \mu\text{m}, 0.012\ \mu\text{m})$, where a very non-equilibrium *pdf* is observed.

5. Conclusions and final remarks

We have developed a DG scheme for BTEs of type (1.1), which takes into account optical-phonon interactions that become dominant under strong energetic conditions. We used the coordinate transformation proposed in [27,4] and changed the collision into an integral-difference operator by using energy band as one of the variables. The Poisson equation is treated by LDG on a mesh that is consistent with the mesh of the DG-BTE scheme. The results are compared to those obtained from a high order WENO scheme simulation. By a local refinement in mesh, we were able to capture the subtle kinetic effects including very non-equilibrium distributions without a great increase of memory allocation and CPU time. The advantage of the DG scheme lies in its potential for implementation on unstructured meshes and for full *hp*-adaptivity. The simple communication pattern of the DG method also makes it a good candidate for the domain decomposition method for the coupled kinetic and macroscopic models.

Appendix A

In this appendix, we collect some technical details for the implementation of the 2D DG-BTE solver. The discussion for 1D solver is similar and omitted here.

A.1. The basis of the finite dimensional function space

In every cell Ω_{ijkmn}, we use piecewise linear polynomials and assume

$$\begin{aligned}\Phi_h(t,x,y,w,\mu,\varphi) = {} & T_{ijkmn}(t) + X_{ijkmn}(t)\frac{2(x-x_i)}{\Delta x_i} + Y_{ijkmn}(t)\frac{2(y-y_j)}{\Delta y_j} \\ & + W_{ijkmn}(t)\frac{2(w-w_k)}{\Delta w_k} + M_{ijkmn}(t)\frac{2(\mu-\mu_m)}{\Delta\mu_m} \\ & + P_{ijkmn}(t)\frac{2(\varphi-\varphi_n)}{\Delta\varphi_n}. \end{aligned} \tag{A.1}$$

It will be useful to note that

$$\begin{aligned}&\Phi_h(t,x,y,w,\mu,\varphi) \\ &= \sum_{k=1}^{N_w}\left[T_{ijkmn}(t) + X_{ijkmn}(t)\frac{2(x-x_i)}{\Delta x_i} + Y_{ijkmn}(t)\frac{2(y-y_j)}{\Delta y_j}\right. \\ &\left. + W_{ijkmn}(t)\frac{2(w-w_k)}{\Delta w_k} + M_{ijkmn}(t)\frac{2(\mu-\mu_m)}{\Delta\mu_m} + P_{ijkmn}(t)\frac{2(\varphi-\varphi_n)}{\Delta\varphi_n}\right]\chi_k(w)\end{aligned}$$

for every $(x,y,w,\mu,\varphi) \in \bigcup_{k=1}^{N_w}\Omega_{ijkmn}$. Here, $\chi_k(w)$ is the characteristic function in the interval $\left[w_{k-\frac{1}{2}}, w_{k+\frac{1}{2}}\right]$.

A.2. Treatment of the collision operator

The gain term of the collisional operator is

$$\begin{aligned}G(\Phi_h)(t,x,y,w) = s(w)\Big\{ & c_0\int_0^{\pi} d\varphi' \int_{-1}^{1} d\mu' \Phi_h(t,x,y,w,\mu',\varphi') \\ & + \int_0^{\pi} d\varphi' \int_{-1}^{1} d\mu' [c_+\Phi_h(t,x,y,w+\gamma,\mu',\varphi') \\ & + c_-\Phi_h(t,x,y,w-\gamma,\mu',\varphi')]\Big\}. \end{aligned} \tag{A.2}$$

Now, we define

$$(\overline{v_h})_{mn}(x,y,w) := \int_{\varphi_{n-\frac{1}{2}}}^{\varphi_{n+\frac{1}{2}}} d\varphi \int_{\mu_{m-\frac{1}{2}}}^{\mu_{m+\frac{1}{2}}} d\mu\, v_h(x,y,w,\mu,\varphi),$$

and, for $\sigma = -\gamma, 0, \gamma$, we have

$$\begin{aligned}&\int_{\Omega_{ijkmn}} v_h(x,y,w,\mu,\varphi)\left[s(w)\int_0^{\pi} d\varphi' \int_{-1}^{1} d\mu' \Phi(t,x,y,w+\sigma,\mu',\varphi')\right] \\ &\quad \times dx\,dy\,dw\,d\mu\,d\varphi \\ &= \int_0^{\pi} d\varphi' \int_{-1}^{1} d\mu' \int_{x_{i-\frac{1}{2}}}^{x_{i+\frac{1}{2}}} dx \int_{y_{j-\frac{1}{2}}}^{y_{j+\frac{1}{2}}} dy \int_{w_{k-\frac{1}{2}}}^{w_{k+\frac{1}{2}}} dw\, s(w) \\ &\quad \times \Phi(t,x,y,w+\sigma,\mu',\varphi')(\overline{v_h})_{mn}(x,y,w) \\ &= \sum_{m'=1}^{N_\mu}\sum_{n'=1}^{N_\varphi} \int_{\Omega_{ijkm'n'}} s(w)\Phi_h(t,x,y,w+\sigma,\mu',\varphi') \\ &\quad \times (\overline{v_h})_{mn}(x,y,w)dx\,dy\,dw\,d\mu'\,d\varphi'. \end{aligned}$$

Now we discuss the following integral for different test function v_h,

$$\begin{aligned}I = & \int_{\Omega_{ijkmn}} v_h(x,y,w,\mu,\varphi)\left[s(w)\int_0^{\pi} d\varphi' \int_{-1}^{1} d\mu' \Phi_h(t,x,y,w+\sigma,\mu',\varphi')\right] \\ & \times dx\,dy\,dw\,d\mu\,d\varphi. \end{aligned}$$

- For $v_h(x,y,w,\mu,\varphi) = 1$,

$$\begin{aligned}I = \sum_{m'=1}^{N_\mu}\sum_{n'=1}^{N_\varphi}\sum_{k'=1}^{N_w}\Delta\mu_{m'}\Delta\varphi_{n'} & \left[T_{ijk'm'n'}(t)\int_{w_{k-\frac{1}{2}}}^{w_{k+\frac{1}{2}}} s(w)\chi_{k'}(w+\sigma)dw\right. \\ & \left. + W_{ijk'm'n'}(t)\int_{w_{k-\frac{1}{2}}}^{w_{k+\frac{1}{2}}} s(w)\frac{2(w+\sigma-w_{k'})}{\Delta w_{k'}}\chi_{k'}(w+\sigma)dw\right]\Delta x_i\Delta y_j\Delta\mu_m\Delta\varphi_n. \end{aligned}$$

- For $v_h(x,y,w,\mu,\varphi) = \frac{2(x-x_i)}{\Delta x_i}$,

$$\begin{aligned}I = {} & \frac{1}{3}\Delta x_i\Delta y_j\Delta\mu_m\Delta\varphi_n\sum_{m'=1}^{N_\mu}\sum_{n'=1}^{N_\varphi}\sum_{k'=1}^{N_w}\Delta\mu_{m'}\Delta\varphi_{n'}X_{ijk'm'n'}(t) \\ & \times\int_{w_{k-\frac{1}{2}}}^{w_{k+\frac{1}{2}}} s(w)\chi_{k'}(w+\sigma)dw. \end{aligned}$$

- For $v_h(x,y,w,\mu,\varphi) = \frac{2(y-y_j)}{\Delta y_j}$,

$$\begin{aligned}I = {} & \frac{1}{3}\Delta x_i\Delta y_j\Delta\mu_m\Delta\varphi_n\sum_{m'=1}^{N_\mu}\sum_{n'=1}^{N_\varphi}\sum_{k'=1}^{N_w}\Delta\mu_{m'}\Delta\varphi_{n'}Y_{ijk'm'n'}(t) \\ & \times\int_{w_{k-\frac{1}{2}}}^{w_{k+\frac{1}{2}}} s(w)\chi_{k'}(w+\sigma)dw. \end{aligned}$$

- For $v_h(x,y,w,\mu,\varphi) = \frac{2(w-w_k)}{\Delta w_k}$,

$$\begin{aligned}I = \sum_{m'=1}^{N_\mu}\sum_{n'=1}^{N_\varphi}\sum_{k'=1}^{N_w}\Delta\mu_{m'}\Delta\varphi_{n'} & \left[T_{ijk'm'n'}(t)\int_{w_{k-\frac{1}{2}}}^{w_{k+\frac{1}{2}}} s(w)\frac{2(w-w_k)}{\Delta w_k}\chi_{k'}(w+\sigma)dw\right. \\ & \left. + W_{ijk'm'n'}(t)\int_{w_{k-\frac{1}{2}}}^{w_{k+\frac{1}{2}}} s(w)\frac{4(w+\sigma-w_k)(w-w_k)}{\Delta w_{k'}\Delta w_k}\chi_{k'}(w+\sigma)dw\right]\Delta x_i\Delta y_j\Delta\mu_m\Delta\varphi_n. \end{aligned}$$

- For $v_h(x,y,w,\mu,\varphi)=\frac{2(\mu-\mu_m)}{\Delta\mu_m}, I=0.$
- For $v_h(x,y,w,\mu,\varphi)=\frac{2(\varphi-\varphi_n)}{\Delta\varphi_n}, I=0.$
  The lost term in the collision operator is

$$2\pi[c_0 s(w)+c_+ s(w-\gamma)+c_- s(w+\gamma)]\Phi(t,x,y,w,\mu,\varphi). \tag{A.3}$$

Let

$$v(w)=2\pi[c_0 s(w)+c_+ s(w-\gamma)+c_- s(w+\gamma)],$$

then we need to evaluate numerically,

$$I'=\int_{\Omega_{ijkmn}} v(w)\Phi_h(t,x,y,w,\mu,\varphi)v_h(x,y,w,\mu,\varphi)dx\,dy\,dw\,d\mu\,d\varphi.$$

- For $v_h(x,y,w,\mu,\varphi)=1$,

$$I'=\Delta x_i\Delta y_j\Delta\mu_m\Delta\varphi_n \times\left[T_{ijkmn}(t)\int_{w_{k-\frac12}}^{w_{k+\frac12}} v(w)dw+W_{ijkmn}(t)\int_{w_{k-\frac12}}^{w_{k+\frac12}} v(w)\frac{2(w-w_k)}{\Delta w_k}dw\right].$$

- For $v_h(x,y,w,\mu,\varphi)=\frac{2(x-x_i)}{\Delta x_i}$,

$$I'=\frac13\Delta x_i\Delta y_j\Delta\mu_m\Delta\varphi_n X_{ijkmn}(t)\int_{w_{k-\frac12}}^{w_{k+\frac12}} v(w)dw.$$

- For $v_h(x,y,w,\mu,\varphi)=\frac{2(y-y_j)}{\Delta y_j}$,

$$I'=\frac13\Delta x_i\Delta y_j\Delta\mu_m\Delta\varphi_n Y_{ijkmn}(t)\int_{w_{k-\frac12}}^{w_{k+\frac12}} v(w)dw.$$

- For $v_h(x,y,w,\mu,\varphi)=\frac{2(w-w_k)}{\Delta w_k}$,

$$I'=\Delta x_i\Delta y_j\Delta\mu_m\Delta\varphi_n\left[T_{ijkmn}(t)\int_{w_{k-\frac12}}^{w_{k+\frac12}} v(w)\frac{2(w-w_k)}{\Delta w_k}dw +W_{ijkmn}(t)\int_{w_{k-\frac12}}^{w_{k+\frac12}} v(w)\frac{4(w-w_k)^2}{(\Delta w_k)^2}dw\right].$$

- For $v_h(x,y,w,\mu,\varphi)=\frac{2(\mu-\mu_m)}{\Delta\mu_m}$,

$$I'=\frac13\Delta x_i\Delta y_j\Delta\mu_m\Delta\varphi_n M_{ijkmn}(t)\int_{w_{k-\frac12}}^{w_{k+\frac12}} v(w)dw.$$

- For $v_h(x,y,w,\mu,\varphi)=\frac{2(\varphi-\varphi_n)}{\Delta\varphi_n}$,

$$I'=\frac13\Delta x_i\Delta y_j\Delta\mu_m\Delta\varphi_n P_{ijkmn}(t)\int_{w_{k-\frac12}}^{w_{k+\frac12}} v(w)dw.$$

A.3. Integrals related to the collisional operator

We need to evaluate (some numerically) the following integrals

$$\int_{w_{k-\frac12}}^{w_{k+\frac12}} s(w)\chi_{k'}(w+\sigma)dw,$$

$$\int_{w_{k-\frac12}}^{w_{k+\frac12}} s(w)\frac{2(w+\sigma-w_{k'})}{\Delta w_{k'}}\chi_{k'}(w+\sigma)dw,$$

$$\int_{w_{k-\frac12}}^{w_{k+\frac12}} s(w)\frac{2(w-w_k)}{\Delta w_k}\chi_{k'}(w+\sigma)dw,$$

$$\int_{w_{k-\frac12}}^{w_{k+\frac12}} s(w)\frac{4(w+\sigma-w_{k'})(w-w_k)}{\Delta w_{k'}\Delta w_k}\chi_{k'}(w+\sigma)dw,$$

$$\int_{w_{k-\frac12}}^{w_{k+\frac12}} v(w)dw,$$

$$\int_{w_{k-\frac12}}^{w_{k+\frac12}} v(w)\frac{2(w-w_k)}{\Delta w_k}dw,$$

$$\int_{w_{k-\frac12}}^{w_{k+\frac12}} v(w)\left[\frac{2(w-w_k)}{\Delta w_k}\right]^2 dw.$$

If we evaluate these integrals by means of numerical quadrature formulas, then it is appropriate to eliminate the singularity of the function $s(w)$ at $w=0$ by change of variables.

$$\int_a^b s(w)dw=\int_a^b\sqrt{w(1+\alpha_K w)}(1+2\alpha_K w)dw =\int_{\sqrt a}^{\sqrt b}\sqrt{1+\alpha_K r^2}(1+2\alpha_K r^2)2r^2\,dr,\quad (w=r^2),$$

$$\int_a^b s(w-\gamma)dw=\int_{a-\gamma}^{b-\gamma} s(\hat w)d\hat w =\int_{\sqrt{a-\gamma}}^{\sqrt{b-\gamma}}\sqrt{1+\alpha_K r^2}(1+2\alpha_K r^2)2r^2\,dr,\quad (w=r^2+\gamma),$$

$$\int_a^b s(w+\gamma)dw=\int_{a+\gamma}^{b+\gamma} s(\bar w)d\bar w =\int_{\sqrt{a+\gamma}}^{\sqrt{b+\gamma}}\sqrt{1+\alpha_K r^2}(1+2\alpha_K r^2)2r^2\,dr,\quad (w=r^2-\gamma).$$

A.4. Integrals related to the free streaming operator

We recall that

$$g_1(\cdot)=c_x\frac{\mu\sqrt{w(1+\alpha_K w)}}{1+2\alpha_K w},$$

$$g_2(\cdot)=c_x\frac{\sqrt{1-\mu^2}\sqrt{w(1+\alpha_K w)}\cos\varphi}{1+2\alpha_K w},$$

$$g_3(\cdot)=-2c_k\frac{\sqrt{w(1+\alpha_K w)}}{1+2\alpha_K w}\left[\mu E_x(t,x,y)+\sqrt{1-\mu^2}\cos\varphi E_y(t,x,y)\right],$$

$$g_4(\cdot)=-c_k\frac{\sqrt{1-\mu^2}}{\sqrt{w(1+\alpha_K w)}}\left[\sqrt{1-\mu^2}E_x(t,x,y)-\mu\cos\varphi E_y(t,x,y)\right],$$

$$g_5(\cdot)=c_k\frac{\sin\varphi}{\sqrt{w(1+\alpha_K w)}\sqrt{1-\mu^2}}E_y(t,x,y).$$

Now, we define:

$$s_1(w)=\frac{\sqrt{w(1+\alpha_K w)}}{1+2\alpha_K w},\quad s_2(w)=\frac{1}{\sqrt{w(1+\alpha_K w)}}.$$

We need to evaluate the integrals.

$$\int_a^b s_1(w)dw=\int_a^b\frac{\sqrt{w(1+\alpha_K w)}}{1+2\alpha_K w}dw=\int_{\sqrt a}^{\sqrt b}\frac{\sqrt{1+\alpha_K r^2}}{1+2\alpha_K r^2}2r^2\,dr,$$

$$\int_a^b s_2(w)dw=\int_a^b\frac{1}{\sqrt{w(1+\alpha_K w)}}dw=\int_{\sqrt a}^{\sqrt b}\frac{2}{\sqrt{1+\alpha_K r^2}}dr,$$

$$\int_a^b s_1(w)\frac{2(w-w_k)}{\Delta w_k}dw=\int_a^b\frac{\sqrt{w(1+\alpha_K w)}}{1+2\alpha_K w}\frac{2(w-w_k)}{\Delta w_k}dw =\int_{\sqrt a}^{\sqrt b}\frac{\sqrt{1+\alpha_K r^2}}{1+2\alpha_K r^2}\frac{2(r^2-w_k)}{\Delta w_k}2r^2\,dr,$$

$$\int_a^b s_2(w)\frac{2(w-w_k)}{\Delta w_k}dw=\int_a^b\frac{1}{\sqrt{w(1+\alpha_K w)}}\frac{2(w-w_k)}{\Delta w_k}dw =\int_{\sqrt a}^{\sqrt b}\frac{2}{\sqrt{1+\alpha_K r^2}}\frac{2(r^2-w_k)}{\Delta w_k}dr,$$

$$\int_a^b s_1(w)\left[\frac{2(w-w_k)}{\Delta w_k}\right]^2 dw=\int_a^b\frac{\sqrt{w(1+\alpha_K w)}}{1+2\alpha_K w}\left[\frac{2(w-w_k)}{\Delta w_k}\right]^2 dw =\int_{\sqrt a}^{\sqrt b}\frac{\sqrt{1+\alpha_K r^2}}{1+2\alpha_K r^2}\left[\frac{2(r^2-w_k)}{\Delta w_k}\right]^2 2r^2\,dr,$$

$$\int_a^b s_2(w)\left[\frac{2(w-w_k)}{\Delta w_k}\right]^2 dw = \int_a^b \frac{1}{\sqrt{w(1+\alpha_K w)}}\left[\frac{2(w-w_k)}{\Delta w_k}\right]^2 dw = \int_{\sqrt{a}}^{\sqrt{b}} \frac{2}{\sqrt{1+\alpha_K r^2}}\left[\frac{2(r^2-w_k)}{\Delta w_k}\right]^2 dr.$$

A.5. Initial condition

Since $measure(\Omega_{ijkmn}) = \Delta x_i\,\Delta y_j\,\Delta w_k\,\Delta\mu_m\,\Delta\varphi_n$, we have

$$\int_{\Omega_{ijkmn}} \Phi_h(0,x,y,w,\mu,\varphi)dx\,dy\,dw\,d\mu\,d\varphi = measure(\Omega_{ijkmn})T_{ijkmn}(0),$$

$$\int_{\Omega_{ijkmn}} \Phi_h(0,x,y,w,\mu,\varphi)\frac{2(x-x_i)}{\Delta x_i}dx\,dy\,dw\,d\mu\,d\varphi = \frac{1}{3}measure(\Omega_{ijkmn})X_{ijkmn}(0),$$

$$\int_{\Omega_{ijkmn}} \Phi_h(0,x,y,w,\mu,\varphi)\frac{2(y-y_j)}{\Delta y_j}dx\,dy\,dw\,d\mu\,d\varphi = \frac{1}{3}measure(\Omega_{ijkmn})Y_{ijkmn}(0),$$

$$\int_{\Omega_{ijkmn}} \Phi_h(0,x,y,w,\mu,\varphi)\frac{2(w-w_k)}{\Delta w_k}dx\,dy\,dw\,d\mu d\varphi = \frac{1}{3}measure(\Omega_{ijkmn})W_{ijkmn}(0),$$

$$\int_{\Omega_{ijkmn}} \Phi_h(0,x,y,w,\mu,\varphi)\frac{2(\mu-\mu_m)}{\Delta\mu_m}dx\,dy\,dw\,d\mu\,d\varphi = \frac{1}{3}measure(\Omega_{ijkmn})M_{ijkmn}(0),$$

$$\int_{\Omega_{ijkmn}} \Phi_h(0,x,y,w,\mu,\varphi)\frac{2(\varphi-\varphi_n)}{\Delta\varphi_n}dx\,dy\,dw\,d\mu\,d\varphi = \frac{1}{3}measure(\Omega_{ijkmn})P_{ijkmn}(0).$$

If, for each (x,y) and (μ,φ),

$$\Phi_h(0,x,y,w,\mu,\varphi) = \begin{cases} F(x,y)s(w)e^{-w} & \text{for } w < w_{N_w+\frac{1}{2}}, \\ 0 \quad \text{otherwise} \end{cases}$$

and

$$F(x,y) = F_{ij}(\text{constant}), \quad \forall (x,y) \in \left[x_{i-\frac{1}{2}}, x_{i+\frac{1}{2}}\right] \times \left[y_{j-\frac{1}{2}}, y_{j+\frac{1}{2}}\right],$$

then it is reasonable to assume

$$T_{ijkmn}(0) = \frac{F_{ij}}{\Delta w_k}\int_{w_{k-\frac{1}{2}}}^{w_{k+\frac{1}{2}}} s(w)e^{-w}dw, \tag{A.4}$$

$$X_{ijkmn}(0) = Y_{ijkmn}(0) = 0, \tag{A.5}$$

$$W_{ijkmn}(0) = 3\frac{F_{ij}}{\Delta w_k}\int_{w_{k-\frac{1}{2}}}^{w_{k+\frac{1}{2}}} s(w)e^{-w}\frac{2(w-w_k)}{\Delta w_k}dw, \tag{A.6}$$

$$M_{ijkmn}(0) = P_{ijkmn}(0) = 0. \tag{A.7}$$

Recalling the definition (2.10) of the dimensionless charge density, we have

$$\rho(0,x,y) = 2\pi F(x,y)\sum_{k=1}^{N_w}\int_{w_{k-\frac{1}{2}}}^{w_{k+\frac{1}{2}}} s(w)e^{-w}dw,$$

which gives a relationship between $F(x,y)$ and the initial charge density ρ.

A.6. Hydrodynamical variables

If $(x,y) \in \left[x_{i-\frac{1}{2}}, x_{i+\frac{1}{2}}\right] \times \left[y_{j-\frac{1}{2}}, y_{j+\frac{1}{2}}\right]$, then

$$\rho_h(t,x,y) = \sum_{k=1}^{N_w}\sum_{m=1}^{N_\mu}\sum_{n=1}^{N_\varphi}\left[T_{ijkmn}(t) + X_{ijkmn}(t)\frac{2(x-x_i)}{\Delta x_i} + Y_{ijkmn}(t)\frac{2(y-y_j)}{\Delta y_j}\right]\Delta w_k\,\Delta\mu_m\,\Delta\varphi_n. \tag{A.8}$$

We define

$$\widehat{T}_{ij}(t) = \sum_{k=1}^{N_w}\sum_{m=1}^{N_\mu}\sum_{n=1}^{N_\varphi} T_{ijkmn}(t)\Delta w_k\,\Delta\mu_m\,\Delta\varphi_n,$$

$$\widehat{X}_{ij}(t) = \sum_{k=1}^{N_w}\sum_{m=1}^{N_\mu}\sum_{n=1}^{N_\varphi} X_{ijkmn}(t)\Delta w_k\,\Delta\mu_m\,\Delta\varphi_n,$$

$$\widehat{Y}_{ij}(t) = \sum_{k=1}^{N_w}\sum_{m=1}^{N_\mu}\sum_{n=1}^{N_\varphi} Y_{ijkmn}(t)\Delta w_k\,\Delta\mu_m\,\Delta\varphi_n.$$

Therefore, for every $(x,y) \in \left[x_{i-\frac{1}{2}}, x_{i+\frac{1}{2}}\right] \times \left[y_{j-\frac{1}{2}}, y_{j+\frac{1}{2}}\right]$,

$$\rho_h(t,x,y) = \widehat{T}_{ij}(t) + \widehat{X}_{ij}(t)\frac{2(x-x_i)}{\Delta x_i} + \widehat{Y}_{ij}(t)\frac{2(y-y_j)}{\Delta y_j}. \tag{A.9}$$

For every $(x,y) \in \left[x_{i-\frac{1}{2}}, x_{i+\frac{1}{2}}\right] \times \left[y_{j-\frac{1}{2}}, y_{j+\frac{1}{2}}\right]$, the approximate momentum in x-direction is

$$\begin{aligned}&\sum_{k=1}^{N_w}\sum_{m=1}^{N_\mu}\sum_{n=1}^{N_\varphi}\Delta\varphi_n[g_{1,km}T_{ijkmn}(t) + g_{1w,km}W_{ijkmn}(t) + g_{1\mu,km}M_{ijkmn}(t)] \\ &+ \left[\sum_{k=1}^{N_w}\sum_{m=1}^{N_\mu}\sum_{n=1}^{N_\varphi}\Delta\varphi_n g_{1,km}X_{ijkmn}(t)\right]\frac{2(x-x_i)}{\Delta x_i} \\ &+ \left[\sum_{k=1}^{N_w}\sum_{m=1}^{N_\mu}\sum_{n=1}^{N_\varphi}\Delta\varphi_n g_{1,km}Y_{ijkmn}(t)\right]\frac{2(y-y_j)}{\Delta y_j},\end{aligned} \tag{A.10}$$

and the approximate momentum in y-direction is

$$\begin{aligned}&\sum_{k=1}^{N_w}\sum_{m=1}^{N_\mu}\sum_{n=1}^{N_\varphi}[g_{2,kmn}T_{ijkmn}(t) + g_{2w,kmn}W_{ijkmn}(t) + g_{2\mu,kmn}M_{ijkmn}(t) + g_{2\varphi,kmn}P_{ijkmn}(t)] \\ &+ \left[\sum_{k=1}^{N_w}\sum_{m=1}^{N_\mu}\sum_{n=1}^{N_\varphi} g_{2,kmn}X_{ijkmn}(t)\right]\frac{2(x-x_i)}{\Delta x_i} \\ &+ \left[\sum_{k=1}^{N_w}\sum_{m=1}^{N_\mu}\sum_{n=1}^{N_\varphi} g_{2,kmn}Y_{ijkmn}(t)\right]\frac{2(y-y_j)}{\Delta y_j},\end{aligned} \tag{A.11}$$

where

$$g_{1,km} = \int_{w_{k-\frac{1}{2}}}^{w_{k+\frac{1}{2}}}\int_{\mu_{m-\frac{1}{2}}}^{\mu_{m+\frac{1}{2}}} g_1(w,\mu)dw\,d\mu,$$

$$g_{1w,km} = \int_{w_{k-\frac{1}{2}}}^{w_{k+\frac{1}{2}}}\int_{\mu_{m-\frac{1}{2}}}^{\mu_{m+\frac{1}{2}}} g_1(w,\mu)\frac{2(w-w_k)}{\Delta w_k}dw\,d\mu,$$

$$g_{1\mu,km} = \int_{w_{k-\frac{1}{2}}}^{w_{k+\frac{1}{2}}}\int_{\mu_{m-\frac{1}{2}}}^{\mu_{m+\frac{1}{2}}} g_1(w,\mu)\frac{2(\mu-\mu_m)}{\Delta\mu_m}dw\,d\mu,$$

$$g_{2,kmn} = \int_{w_{k-\frac{1}{2}}}^{w_{k+\frac{1}{2}}}\int_{\mu_{m-\frac{1}{2}}}^{\mu_{m+\frac{1}{2}}}\int_{\varphi_{n-\frac{1}{2}}}^{\varphi_{n+\frac{1}{2}}} g_2(w,\mu,\varphi)dw\,d\mu\,d\varphi,$$

$$g_{2w,kmn} = \int_{w_{k-\frac{1}{2}}}^{w_{k+\frac{1}{2}}} \int_{\mu_{m-\frac{1}{2}}}^{\mu_{m+\frac{1}{2}}} \int_{\varphi_{n-\frac{1}{2}}}^{\varphi_{n+\frac{1}{2}}} g_2(w,\mu,\varphi)\frac{2(w-w_k)}{\Delta w_k} dw\,d\mu\,d\varphi,$$

$$g_{2\mu,kmn} = \int_{w_{k-\frac{1}{2}}}^{w_{k+\frac{1}{2}}} \int_{\mu_{m-\frac{1}{2}}}^{\mu_{m+\frac{1}{2}}} \int_{\varphi_{n-\frac{1}{2}}}^{\varphi_{n+\frac{1}{2}}} g_2(w,\mu,\varphi)\frac{2(\mu-\mu_m)}{\Delta \mu_m} dw\,d\mu\,d\varphi,$$

$$g_{2\varphi,kmn} = \int_{w_{k-\frac{1}{2}}}^{w_{k+\frac{1}{2}}} \int_{\mu_{m-\frac{1}{2}}}^{\mu_{m+\frac{1}{2}}} \int_{\varphi_{n-\frac{1}{2}}}^{\varphi_{n+\frac{1}{2}}} g_2(w,\mu,\varphi)\frac{2(\varphi-\varphi_n)}{\Delta \varphi_n} dw\,d\mu\,d\varphi.$$

Analogously, the energy multiplied by the charge density $\rho_h(t,x,y)$ is

$$\begin{aligned}
&\sum_{k=1}^{N_w}\sum_{m=1}^{N_\mu}\sum_{n=1}^{N_\varphi}\Delta\varphi_n\Delta\mu_m\left[w_k\Delta w_k T_{ijkmn}(t) + \frac{(\Delta w_k)^2}{6}W_{ijkmn}(t)\right] \\
&\quad + \left[\sum_{k=1}^{N_w}\sum_{m=1}^{N_\mu}\sum_{n=1}^{N_\varphi}\Delta\varphi_n\Delta\mu_m w_k\Delta w_k X_{ijkmn}(t)\right]\frac{2(x-x_i)}{\Delta x_i} \\
&\quad + \left[\sum_{k=1}^{N_w}\sum_{m=1}^{N_\mu}\sum_{n=1}^{N_\varphi}\Delta\varphi_n\Delta\mu_m w_k\Delta w_k Y_{ijkmn}(t)\right]\frac{2(y-y_j)}{\Delta y_j} \qquad \text{(A.12)}
\end{aligned}$$

for every $(x,y) \in \left[x_{i-\frac{1}{2}}, x_{i+\frac{1}{2}}\right] \times \left[y_{j-\frac{1}{2}}, y_{j+\frac{1}{2}}\right]$.

References

[1] D. Arnold, F. Brezzi, B. Cockburn, L. Marini, Unified analysis of discontinuous Galerkin methods for elliptic problems, SIAM J. Numer. Anal. 39 (2002) 1749–1779.

[2] M.J. Caceres, J.A. Carrillo, I.M. Gamba, A. Majorana, C.-W. Shu, Deterministic kinetic solvers for charged particle transport in semiconductor devices, in: C. Cercignani, E. Gabetta (Eds.), Transport Phenomena and Kinetic Theory Applications to Gases Semiconductors Photons and Biological Systems, Birkhäuser, 2006, pp. 151–171.

[3] J.A. Carrillo, I.M. Gamba, A. Majorana, C.-W. Shu, A WENO-solver for 1D non-stationary Boltzmann–Poisson system for semiconductor devices, J. Comput. Electron. 1 (2002) 365–375.

[4] J.A. Carrillo, I.M. Gamba, A. Majorana, C.-W. Shu, A direct solver for 2D non-stationary Boltzmann–Poisson systems for semiconductor devices: a MESFET simulation by WENO-Boltzmann schemes, J. Comput. Electron. 2 (2003) 375–380.

[5] J.A. Carrillo, I.M. Gamba, A. Majorana, C.-W. Shu, A WENO-solver for the transients of Boltzmann–Poisson system for semiconductor devices. Performance and comparisons with Monte Carlo methods, J. Comput. Phys. 184 (2003) 498–525.

[6] J.A. Carrillo, I.M. Gamba, A. Majorana, C.-W. Shu, 2D semiconductor device simulations by WENO-Boltzmann schemes: efficiency, boundary conditions and comparison to Monte Carlo methods, J. Comput. Phys. 214 (2006) 55–80.

[7] Z. Chen, B. Cockburn, C. Gardner, J. Jerome, Quantum hydrodynamic simulation of hysteresis in the resonant tunneling diode, J. Comput. Phys. 274 (1995) 274–280.

[8] Z. Chen, B. Cockburn, J.W. Jerome, C.-W. Shu, Mixed-RKDG finite element methods for the 2-d hydrodynamic model for semiconductor device simulation, VLSI Design 3 (1995) 145–158.

[9] Y. Cheng, I. Gamba, A. Majorana, C.-W. Shu, A discontinuous Galerkin solver for full-Band Boltzmann–Poisson models, in: The Proceeding of IWCE 13, 2009, pp. 211–214.

[10] Y. Cheng, I. Gamba, A. Majorana, C.-W. Shu, Discontinuous Galerkin solver for Boltzmann–Poisson transients, J. Comput. Electron. 7 (2008) 119–123.

[11] Y. Cheng, I.M. Gamba, A. Majorana, C.-W. Shu, Discontinuous Galerkin solver for the semiconductor Boltzmann Equation, in: T. Grasser, S. Selberherr (Eds.), SISPAD 07, Springer, 2007, pp. 257–260.

[12] B. Cockburn, B. Dong, An analysis of the minimal dissipation local discontinuous Galerkin method for convection–diffusion problems, J. Sci. Comput. 32 (2007) 233–262.

[13] B. Cockburn, S. Hou, C.-W. Shu, The Runge–Kutta local projection discontinuous Galerkin finite element method for conservation laws IV: the multidimensional case, Math. Comput. 54 (1990) 545–581.

[14] B. Cockburn, S.-Y. Lin, C.-W. Shu, TVB Runge–Kutta local projection discontinuous Galerkin finite element method for conservation laws III: one dimensional systems, J. Comput. Phys. 84 (1989) 90–113.

[15] B. Cockburn, C.-W. Shu, TVB Runge–Kutta local projection discontinuous Galerkin finite element method for conservation laws II: general framework, Math. Comput. 52 (1989) 411–435.

[16] B. Cockburn, C.-W. Shu, The Runge–Kutta local projection P1-discontinuous Galerkin finite element method for scalar conservation laws, Math. Model. Numer. Anal. 25 (1991) 337–361.

[17] B. Cockburn, C.-W. Shu, The Runge–Kutta discontinuous Galerkin method for conservation laws V: multidimensional systems, J. Comput. Phys. 141 (1998) 199–224.

[18] B. Cockburn, C.-W. Shu, The local discontinuous Galerkin method for time-dependent convection–diffusion systems, SIAM J. Numer. Anal. 35 (1998) 2440–2463.

[19] B. Cockburn, C.-W. Shu, Runge–Kutta discontinuous Galerkin methods for convection-dominated problems, J. Sci. Comput. 16 (2001) 173–261.

[20] E. Fatemi, F. Odeh, Upwind finite difference solution of Boltzmann equation applied to electron transport in semiconductor devices, J. Comput. Phys. 108 (1993) 209–217.

[21] D.K. Ferry, Semiconductors, Maxwell MacMillian, New-York, 1991.

[22] M. Galler, A. Majorana, Deterministic and stochastic simulation of electron transport in semiconductors, Bull. Inst. Math., Acad. Sinica (New Series) 2 (2) (2007) 349–365. 6th MAFPD (Kyoto) special issue.

[23] C. Jacoboni, P. Lugli, The Monte Carlo Method for Semiconductor Device Simulation, Spring-Verlag, Wien-New York, 1989.

[24] M. Lundstrom, Fundamentals of Carrier Transport, Cambridge University Press, Cambridge, 2000.

[25] Y.-X. Liu, C.-W. Shu, Local discontinuous Galerkin methods for moment models in device simulations: formulation and one dimensional results, J. Comput. Electron. 3 (2004) 263–267.

[26] Y.-X. Liu, C.-W. Shu, Local discontinuous Galerkin methods for moment models in device simulations: performance assessment and two dimensional results, Appl. Numer. Math. 57 (2007) 629–645.

[27] A. Majorana, R. Pidatella, A finite difference scheme solving the Boltzmann–Poisson system for semiconductor devices, J. Comput. Phys. 174 (2001) 649–668.

[28] P.A. Markowich, C. Ringhofer, C. Schmeiser, Semiconductor Equations, Springer-Verlag, New York, 1990.

[29] K. Tomizawa, Numerical Simulation of Sub Micron Semiconductor Devices, Artech House, Boston, 1993.

[30] T. Zhou, Y. Li, C.-W. Shu, Numerical comparison of WENO finite volume and Runge–Kutta discontinuous Galerkin methods, J. Sci. Comput. 16 (2001) 145–171.

[31] J.M. Ziman, Electrons and Phonons. The Theory of Transport Phenomena in Solids, Oxford University Press, Oxford, 2000.